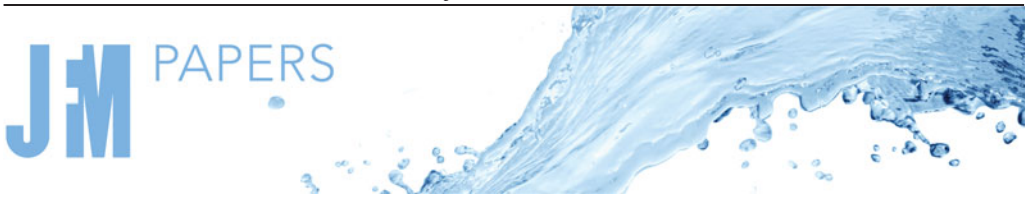
CrossMark

J. Fluid Mech. (2021), *vol*. 923, A7, doi:10.1017/jfm.2021.522



Exact coherent structures and shadowing in turbulent Taylor–Couette flow

Michael C. Krygier[1], **Joshua L. Pughe-Sanford**[1] **and Roman O. Grigoriev**[1],†

[1]School of Physics, Georgia Institute of Technology, Atlanta, GA 30332, USA

(Received 14 January 2021; revised 25 April 2021; accepted 7 June 2021)

We investigate a theoretical framework for modelling fluid turbulence based on the formalism of exact coherent structures (ECSs). Although highly promising, existing evidence for the role of ECSs in turbulent flows is largely circumstantial and comes primarily from idealized numerical simulations. In particular, it remains unclear whether three-dimensional turbulent flows in experiment shadow any ECSs. In order to conclusively answer this question, a hierarchy of ECSs should be computed on a domain and with boundary conditions exactly matching experiment. The present study makes the first step in this direction by investigating a small-aspect-ratio Taylor–Couette flow with naturally periodic boundary conditions in the azimuthal direction. We describe the structure of the chaotic set underlying turbulent flow driven by counter-rotating cylinders and present direct numerical evidence for shadowing of a collection of unstable relative periodic orbits and a travelling wave, setting the stage for further experimental tests of the framework.

Key words: chaos, nonlinear dynamical systems, turbulence theory

1. Introduction

Fluid turbulence has a unique place in science and engineering, due to both its ubiquity and tremendous practical importance as well as its resistance to progress despite a long history of systematic investigation. A statistical description, which dominated early theoretical studies, brought some advances, such as the Kolmogorov's scaling law (Kolmogorov 1941) and the law of the wall (Von Kármán 1930; Nikuradse 1932). These advances, however, are based on general concepts such as dimensional analysis, spatial uniformity and/or isotropy, that are not directly related to the equations governing fluid flow and shed little light onto the nature of the turbulent cascades or momentum transport in wall-bounded flows. Moreover, statistical approaches provide minimal insight into the prediction and control of fluid turbulence.

† Email address for correspondence: romgrig@gatech.edu

© The Author(s), 2021. Published by Cambridge University Press

https://doi.org/10.1017/jfm.2021.522 Published online by Cambridge University Press

Existing statistical models of fluid turbulence fail to predict even such simple quantities as the mean energy dissipation (e.g. in isotropic turbulence) or momentum flux (e.g. in a wall-bounded flow). The calculation of the friction coefficient for pipe flow turbulence is a good example, where one has to rely on empirically derived Moody charts (Moody 1944). Statistical description also fails to account for the presence of coherent structures, which are well known to play an important role in turbulence (Hussain 1983). Indeed, coherent structures break both spatial uniformity and isotropy and introduce new spatial and temporal scales, invalidating the entire foundation of statistical description.

The most promising alternative approach is to build a dynamical description of turbulence firmly based on the equations governing fluid flow. Unlike other classical field theories, such as electromagnetism, whose governing equations are linear, fluid turbulence is governed by the Navier–Stokes equation which is strongly nonlinear, making analytical solutions intractable. Recent advances in numerical methods brought a realization that coherent structures represent unstable solutions of Navier–Stokes with simple temporal dependence, with the earliest example provided by Nagata (1990). This started a revolution in our understanding of fluid turbulence (Kawahara, Uhlmann & Van Veen 2012). Termed exact coherent structures (ECSs), such solutions have been shown to play a key role in the transition from laminar flow to turbulence (Kerswell 2005; Eckhardt *et al.* 2008) and self-sustaining processes in boundary layers (Waleffe & Wang 2005). In some cases, a single ECS was found to reproduce certain statistical properties of weakly turbulent flow. A time-periodic solution obtained by Kawahara & Kida (2001) for plane Couette flow was found to reproduce, with fairly high accuracy, both the mean flow profile and the fluctuations in all three components of the velocity.

It is, therefore, natural to ask whether these results are coincidental, or some collection of ECSs can in fact provide a dynamical and statistical description of fluid turbulence. The idea that turbulence can be thought of as a deterministic walk through a repertoire of patterns (which we now associate with different ECSs) goes back to Eberhard Hopf (Hopf 1942, 1948). In Hopf's view, the snapshot of turbulent flow in the physical space corresponds to a point in the associated infinite-dimensional state (or phase) space. This point traces out a one-dimensional trajectory as the flow evolves in time. This trajectory is confined, due to dissipation, to a finite-dimensional set embedded within this state space. This set can be either an attractor (for sustained turbulence) or a repeller (for transient turbulence).

It took two more decades to flesh out the details of Hopf's picture, when mathematical foundations of deterministic chaos, geometry of chaotic sets and ergodic theory were developed (Lorenz 1963; Mandelbrot 1967; Arnold & Avez 1968). In particular, for uniformly hyperbolic chaotic systems without continuous symmetries, unstable periodic orbits (UPOs) are dense in the chaotic set (Gaspard 2005), which has two important implications. The first one is dynamical: chaotic trajectories shadow nearby UPOs. The second one is statistical: temporal averages over a chaotic trajectory can be computed as a sum over an infinite hierarchy of UPOs (Arnold & Avez 1968), with the weight of each term predicted by periodic orbit theory (Auerbach *et al.* 1987; Cvitanović 1988; Lan 2010).

Turbulent fluid flows are chaotic, at least in so far as the sensitive dependence on initial conditions is concerned, so it is natural to ask whether the properties of shadowing and ergodicity also apply to turbulence. Originally conjectured by Hopf, the shadowing property is widely assumed (Cvitanović 2013) in the studies exploring the ECS-based framework, although there is very little direct evidence in its favour.

Most of the evidence for turbulent flows visiting neighbourhoods of ECSs has been obtained using numerical simulations of minimal flow units and, therefore, has to be

https://doi.org/10.1017/jfm.2021.522 Published online by Cambridge University Press

taken with a pinch of salt. For instance, unstable equilibria and UPOs were found to be visited in forced two-dimensional flow (Kazantsev 1998; Chandler & Kerswell 2013; Lucas & Kerswell 2015), isotropic turbulence (van Veen, Kida & Kawahara 2006) and plane Couette flow (Cvitanović & Gibson 2010; Kreilos & Eckhardt 2012). Travelling waves (TWs) were found to be visited in plane Poiseuille flow (Park & Graham 2015) and pipe flow (Kerswell & Tutty 2007; Schneider, Eckhardt & Vollmer 2007; Dennis & Sogaro 2014) and relative periodic orbits (RPOs) in pipe flow (Willis, Cvitanović & Avila 2013; Budanur *et al.* 2017). Experiments provide more direct and solid evidence. For instance, TWs were found to be visited in pipe flows (Hof *et al.* 2004; De Lozar *et al.* 2012) and unstable equilibria in forced quasi-two-dimensional flows (Suri *et al.* 2017, 2018).

Visits by turbulence to a neighbourhood of an ECS, however, do not imply shadowing, since, in practice, no ECSs are visited particularly closely. Shadowing requires that turbulent flow remain in the neighbourhood of an ECS for an extended interval of time comparable to the characteristic escape time. It also requires that turbulent flow evolve in the same manner as the ECS. Such evidence is currently limited to UPOs in flows without continuous symmetries, e.g. Kolmogorov flow in two dimensions (Suri *et al.* 2020) and three dimensions (Yalnız, Hof & Budanur 2020). However, it is not completely understood how the presence of symmetries affects the shadowing property.

To sum up, while a dynamical description of fluid turbulence based on ECSs is promising, it is yet to be properly validated in both numerical and experimental settings, especially for flows with continuous symmetries. A key challenge is the disconnect between experiments that are conducted on large spatial domains and typically for open flows such as pipe, channel or plane Couette flow and numerics: ECSs are typically computed on minimal flow units with unphysical (e.g. spatially periodic) boundary conditions and/or under unrealistic constraints (e.g. in highly symmetric subspaces). To ensure an 'apples-to-apples' comparison, the dynamical description should be validated in a geometry and under conditions where numerical simulations match experiment as closely as possible. Hence, this study focuses on a weakly turbulent Taylor–Couette flow (TCF) between concentric cylinders, which is easy to realize in practice. This is a closed flow whose boundary conditions in the azimuthal direction are naturally periodic, reflecting continuous rotational symmetry. Furthermore, we do not restrict ECSs to lie in any symmetry subspace.

The TCF considered in this study is characterized by four non-dimensional parameters. Two of these are geometrical: $\Gamma = h/d$ and $\eta = r_i/r_o$, where h is the height of the fluid layer and r_i and r_o are the radii of the inner and outer cylinder, respectively, as shown in figure 1. The other two are the Reynolds numbers: $Re_i = \Omega_i r_i d/\nu$ and $Re_o = \Omega_o r_o d/\nu$, where $d = r_o - r_i$ is the gap between the cylinders, ν is the kinematic viscosity of the fluid and Ω_i and Ω_o are the angular velocities of the two cylinders. We focus on flows driven by counter-rotating cylinders ($Re_i = 1200$, $Re_o = -1200$) in the wide-gap ($\eta = 0.5$), small-aspect-ratio ($\Gamma = 1$) geometry with stationary end-caps.

Previous studies of wide-gap, small-aspect-ratio TCF mainly focused on the flows driven by inner cylinder rotation with the outer cylinder and end-caps being stationary. The bifurcations between steady flows associated with the changes in Re_i, Γ and η have been studied by Benjamin & Mullin (1981), Mullin (1982), Cliffe (1983), Aitta, Ahlers & Cannell (1985), Pfister *et al.* (1988) and Mullin, Toya & Tavener (2002). Time-dependent flows have been investigated by Lorenzen, Pfister & Mullin (1983), Pfister, Schulz & Lensch (1991) and Furukawa *et al.* (2002). The onset of turbulent flows has been considered by Streett & Hussaini (1991) and Pfister, Buzug & Enge (1992) for $\Gamma > 1$, Marques & Lopéz (2006) for $\Gamma = 1$, and Buzug, Von Stamm & Pfister (1992) and

https://doi.org/10.1017/jfm.2021.522 Published online by Cambridge University Press

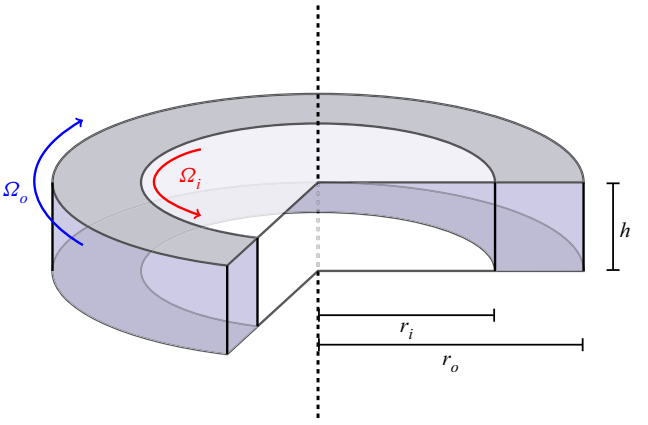


Figure 1. Geometry of the TCF driven by counter-rotating cylinders. The fluid domain is shaded purple.

Buzug, von Stamm & Pfister (1993) for $\Gamma < 1$. The effect of the outer cylinder rotation ($Re_o \neq 0$) on the bifurcation sequence was considered by Schulz, Pfister & Tavener (2003) and Altmeyer *et al.* (2012), but neither study explored Reynolds numbers sufficiently high to observe turbulent flows.

Turbulence in counter-rotating TCF has been investigated mainly in small-gap ($0.9 \lesssim \eta < 1$), large-aspect-ratio ($\Gamma \gg 1$) geometry (Coles 1965; Andereck, Liu & Swinney 1986). A number of TWs, both stable and unstable, have been identified in this regime for $Re_o \lesssim -1200$. These TWs take the shape of rotating spiral waves (Meseguer *et al.* 2009), ribbons (Deguchi & Altmeyer 2013) or spatially localized vortex pairs (Deguchi, Meseguer & Mellibovsky 2014). However, no unstable RPOs of TCF have been found so far.

The main objective of the present numerical study is to validate the key assumptions which underlie the dynamical description of fluid turbulence in a setting which is straightforward to replicate in experiment (Hochstrate *et al.* 2010; Heise *et al.* 2013; Hoffmann *et al.* 2013). Specifically, we are looking to compute a library of ECSs (both TWs and RPOs) that are dynamically prominent and analyse turbulent flows for close passes to each ECS to identify shadowing events, if there are any. The paper is structured as follows. Numerical methods for solving the Navier–Stokes equation and computing ECSs are described in § 2. Our results are presented in § 3 and analysed in § 4. Finally, § 5 presents our conclusions.

2. Mathematical formulation

2.1. *Direct numerical simulation*

The flow is governed by the Navier–Stokes equation and the incompressibility condition which can be written in non-dimensional form using the gap d and the diffusive time scale d^2/ν as the length and time scale, respectively,

$$\left.\begin{aligned} \partial_t \boldsymbol{u} + (\boldsymbol{u}\cdot\nabla)\boldsymbol{u} &= -\nabla p + \nabla^2 \boldsymbol{u}, \\ \nabla\cdot\boldsymbol{u} &= 0. \end{aligned}\right\} \tag{2.1}$$

https://doi.org/10.1017/jfm.2021.522 Published online by Cambridge University Press

Here $\boldsymbol{u} = (u_r, u_\theta, u_z)$ and p are the non-dimensional velocity and pressure. No-slip boundary conditions are imposed on all the walls,

$$\left.\begin{aligned} \boldsymbol{u}(r_i, \theta, z, t) &= (0, Re_i, 0), \\ \boldsymbol{u}(r_o, \theta, z, t) &= (0, Re_o, 0), \\ \boldsymbol{u}(r, \theta, \pm h/2, t) &= (0, 0, 0). \end{aligned}\right\} \tag{2.2}$$

The last relation describes the boundary conditions at the top and bottom of the fluid layer.

Direct numerical simulations (known as DNS) of TCF were performed using a pseudospectral code (Avila *et al.* 2008; Mercader, Batiste & Alonso 2010; Avila 2012) which solves the governing equations in cylindrical coordinates (r, θ, z). The velocity field $\boldsymbol{u}$ at location (r, θ, z) and time t is given by

$$\boldsymbol{u}(r, \theta, z, t) = \mathrm{Re} \sum_{k=0}^{N_r} \sum_{l=0}^{N_z} \sum_{m=0}^{N_\theta/2} \boldsymbol{U}^{klm}(t) T_k(\rho) T_l(\zeta) \mathrm{e}^{\mathrm{i}m\theta}, \tag{2.3}$$

where $\rho = (2r - r_i - r_o)/d$ and $\zeta = 2z/h$. N_r, N_z and N_θ are the number of spectral modes in the three coordinate directions, $T_k(\cdot)$ is the Chebyshev polynomial of order k and the real part is denoted by Re. The solution is advanced in time using a second-order stiffly stable time-splitting scheme (Hugues & Randriamampianina 1998). Advection terms are evaluated on the spatial grid (r_k, z_l, θ_m) in physical space, where

$$\left.\begin{aligned} r_k &= \frac{(r_o - r_i)\cos(k\pi/N_r) + r_i + r_o}{2}, \quad k = 0, \ldots, N_r, \\ z_l &= \frac{\Gamma \cos(l\pi/N_z)}{2}, \quad l = 0, \ldots, N_z, \end{aligned}\right\} \tag{2.4}$$

are Chebyshev collocation points and $\theta_m = 2\pi m/N_\theta$ with $m = 0, \ldots, N_\theta - 1$. The Helmholtz and Poisson equations are solved efficiently using a complete diagonalization of the operators in both the radial and axial direction for each Fourier mode (Orszag & Patera 1983).

We set $N_r = 32$, $N_\theta = 128$, $N_z = 48$ (which corresponds to $3(N_r + 1)(N_z + 1)N_\theta = 620\,928$ degrees of freedom) and used a time step $\mathrm{d}t = O(10^{-6})$ to accurately resolve the spatial structure and temporal dependence of turbulent flow and all computed ECSs. The spatial resolution was chosen such that the magnitude of the spectral coefficients $\boldsymbol{U}^{klm}$ decreases by at least four orders of magnitude for ECSs (and at least three orders of magnitude for turbulent flows) as k, l or m increases from the smallest to the largest value.

2.2. *Computation of ECSs*

Under the boundary conditions (2.2), TCF is invariant under arbitrary rotations R_ϕ about the z-axis, and a reflection K_z about the midplane $z = 0$, where

$$R_\phi \boldsymbol{u}(r, \theta, z, t) = \boldsymbol{u}(r, \theta + \phi, z, t), \tag{2.5}$$

$$K_z \boldsymbol{u}(r, \theta, z, t) = (u_r, u_\theta, -u_z)(r, \theta, -z, t). \tag{2.6}$$

These transformations form a symmetry group $\mathcal{G} = \mathrm{SO}(2) \times \mathrm{Z}_2$. The presence of continuous rotational symmetry and the lack of reflection symmetry in θ imply that the dynamically relevant ECSs in TCF are relative, e.g. relative periodic orbits (RPOs) and

https://doi.org/10.1017/jfm.2021.522 Published online by Cambridge University Press

relative equilibria (TWs), which correspond to time-periodic and stationary states in a corotating reference frame. In particular, RPOs satisfy

$$\boldsymbol{u}(T) - R_{\Phi}\boldsymbol{u}(0) = \boldsymbol{0}, \tag{2.7}$$

where Φ and T are the solution's rotational shift and period, respectively. The angular velocity of this corotating reference frame is $\Omega = \Phi/T$. The TWs also satisfy (2.7) for $T = \Phi/\Omega$ at arbitrary Φ. For both RPOs and TWs, some of which have an N-fold discrete rotational symmetry, we arbitrarily restrict $0 \leq \Phi < 2\pi/N$ to make the definition of rotational shift unique. To find an ECS, the nonlinear equation (2.7) is solved for $\boldsymbol{u}(0)$, T and/or Φ using a custom Newton–GMRES solver that takes advantage of a hookstep algorithm (Viswanath 2007, 2009). A relative residual

$$\varepsilon = \frac{\|\boldsymbol{u}(T) - R_{\Phi}\boldsymbol{u}(0)\|}{\|\boldsymbol{u}(0)\|}, \tag{2.8}$$

was used as the stopping condition for the solver: solutions are considered converged for $\varepsilon < 10^{-11}$. A large set of initial conditions for the solver was generated using the natural measure of the flow, as described below.

Turbulent flow was established using the following protocol. With fluid initially stationary in the entire flow domain, the outer cylinder angular velocity was set to a value Ω_o corresponding to the target $Re_o = -1200$ (with the inner cylinder stationary). The flow was then allowed to evolve for 8.8 time units until a (steady and azimuthally uniform) asymptotic state was established. All the Fourier modes except $m = 0$ were then weakly perturbed in order to break the azimuthal symmetry of the flow, after which the inner cylinder angular velocity was set to a value Ω_i corresponding to the target $Re_i = 1200$. The flow was then evolved for 1.6 time units until a statistically stationary state was reached.

Different turbulent field snapshots were then used as initial conditions to the Newton solver to generate a set of ECSs. To increase the likelihood that the computed ECSs are dynamically relevant, we initialized the Newton solver using deep minima of the recurrence function (Kawahara & Kida 2001; Viswanath 2007; Cvitanović & Gibson 2010)

$$G(t, \tau) = \min_{\phi} \left\| \boldsymbol{u}(t + \tau) - R_{\phi}\boldsymbol{u}(t) \right\|, \tag{2.9}$$

where $\|\cdot\|$ is the L_2-norm. Some of these minima correspond to close passes to RPOs or TWs, and the corresponding flow fields $\boldsymbol{u}(t)$, time delays τ and rotation angles ϕ represent good initial conditions for the solver. An alternative approach to identifying dynamically relevant initial conditions relies on dynamic mode decomposition (Page & Kerswell 2020). Converged solutions were also numerically continued in Re_i using pseudo-arclength continuation (Allgower & Georg 2003); some branches turned around, yielding several additional solutions. For this reason, all of the solutions used in this study were computed for $Re_i = 1200 \pm 3$. Their properties are summarized in table 1.

We used the shortest ECS (RPO_{06}) to verify that our numerical solutions are fully resolved. Specifically, after converging this solution using the standard spatial and temporal discretization, we recomputed it using a finer discretization and used the corresponding relative residual (2.8) to quantify the accuracy of the computed solution. Doubling the spatial resolution in all directions, while keeping the temporal resolution the same, yielded an acceptably small value $\varepsilon = 6.1 \times 10^{-4}$. Doubling the temporal resolution, while keeping the spatial resolution the same, yielded an even smaller value $\varepsilon = 1.2 \times 10^{-6}$.

https://doi.org/10.1017/jfm.2021.522 Published online by Cambridge University Press

n	$\boldsymbol{u}_n$	T	Φ	N_λ^u	γ_n^{-1}	$\min_t D_n^1(t)$	$\min_t D_n^2(t)$	$\min_t D_n^3(t)$	Discrete symmetry
1	TW_{01}	0.1305	π	10	0.0121	0.19	1.17	—	$K_zR_{\pi/2}$
2	TW_{02}	0.0127	π	10	0.0026	1.43	0.68	0.27	R_π
3	TW_{03}	0.0459	2π	43	0.0004	1.37	1.58	—	K_zR_π
4	RPO_{01}	0.0159	0.3541	4	0.0228	0.18	1.16	—	$K_zR_{\pi/2}$
5	RPO_{02}	0.0501	0.8275	9	0.0063	0.22	1.15	—	—
6	RPO_{03}	0.0506	0.8817	4	0.0095	0.18	1.16	—	—
7	RPO_{04}	0.0512	0.9676	5	0.0205	0.22	1.13	—	—
8	RPO_{05}	0.0262	3.4118	5	0.0227	0.14	1.12	—	—
9	RPO_{06}	0.0063	3.2688	6	0.0247	0.22	1.17	—	—
10	RPO_{07}	0.0213	0.1581	4	0.0210	0.30	1.15	—	R_π
11	RPO_{08}	0.0493	0.9091	8	0.0124	0.20	1.16	—	—
12	RPO_{09}	0.0191	3.4949	3	0.0214	0.23	1.16	—	—
13	RPO_{10}	0.0194	3.4615	4	0.0152	0.24	1.15	—	—
14	RPO_{11}	0.0196	3.4270	5	0.0159	0.23	1.14	—	—
15	RPO_{12}	0.0217	0.1442	5	0.0193	0.30	1.16	—	R_π
16	RPO_{13}	0.0081	1.1617	9	0.0051	1.35	0.77	0.27	R_π
17	RPO_{14}	0.0446	5.0016	9	0.0077	1.45	0.88	0.28	—
18	RPO_{15}	0.0073	1.3298	10	0.0045	1.41	0.70	0.18	R_π
19	RPO_{16}	0.0063	1.6429	10	0.0039	1.52	1.03	0.39	—
20	RPO_{17}	0.0121	0.3186	15	0.0016	1.53	1.01	0.58	R_π
21	RPO_{18}	0.0558	2.2912	7	0.0084	1.44	0.82	0.22	—
22	RPO_{19}	0.0451	0.7489	12	0.0021	0.42	1.31	—	—
23	RPO_{20}	0.0361	3.9396	9	0.0084	1.42	0.72	0.24	—

Table 1. Properties of ECSs found in TCF for $\Gamma = 1$, $\eta = 0.5$, $Re_i \approx 1200$ and $Re_o = -1200$: the temporal period T and shift Φ, the number of unstable directions N_λ^u, the inverse of the escape rate γ_n^{-1}, the minimal distance to the turbulent trajectory in lobes 1, 2 and 3, and the discrete symmetries, if any.

3. Results

3.1. *ECSs and state space geometry*

It is easier to understand the state space geometry for this problem and the structure of the chaotic set associated with turbulent flow using coordinates (observables) that are invariant under rotation around the axis. We found the following coordinates to provide a convenient projection: the normalized energy

$$\mathcal{E} = \frac{1}{Re^2 V}\int_V \boldsymbol{u}^2 \,\mathrm{d}V, \tag{3.1}$$

rate of energy dissipation

$$\mathcal{D} = \frac{1}{Re^2 V}\int_V \boldsymbol{\omega}^2 \,\mathrm{d}V \tag{3.2}$$

and helicity

$$\mathcal{H} = \frac{1}{Re^2 V}\int_V \boldsymbol{u}\cdot\boldsymbol{\omega} \,\mathrm{d}V. \tag{3.3}$$

Here $Re = |Re_i - Re_o|/2$ is the characteristic scale for the velocity, V is the volume of the flow domain and $\boldsymbol{\omega} = \boldsymbol{\nabla}\times\boldsymbol{u}$ is the vorticity. Note that $\mathcal{E}$ and $\mathcal{D}$ are invariant under both

https://doi.org/10.1017/jfm.2021.522 Published online by Cambridge University Press

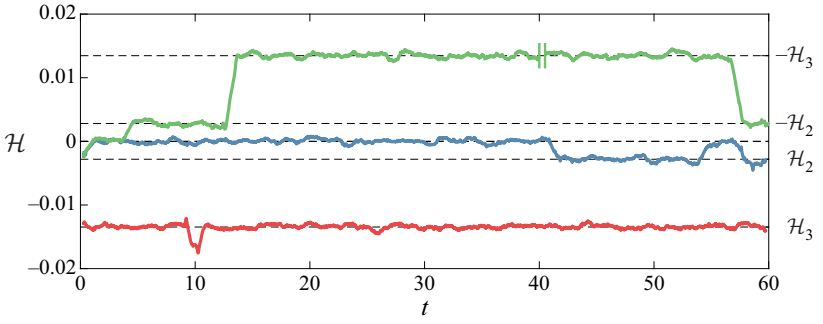


Figure 2. Helicity for $\boldsymbol{u}^a(t)$ (blue), $\boldsymbol{u}^b(t)$ (red), $\boldsymbol{u}^c(t)$ (green). Shown is the running average taken over a window of one time unit. Note that 10 time units are removed from the signal of $\boldsymbol{u}^c(t)$ at $t = 40$, during which the flow remains in lobe 3. The mean helicity of each lobe is illustrated with black dashed lines.

R_ϕ and K_z, while $\mathcal{H}$ is invariant under R_ϕ and changes sign under K_z. The running average of helicity for the turbulent flow initialized as described in the previous section is shown in figure 2 as a blue curve. It is clear that this turbulent trajectory (we will refer to it as $\boldsymbol{u}^a(t)$) explores distinct but connected regions of state space. For $1 \lesssim t \lesssim 40$ and $53 \lesssim t \lesssim 57$, $\boldsymbol{u}^a(t)$ is confined to the part of the chaotic set (which we will refer to as lobe 1) that is centred at $\mathcal{H} = 0$. For $41 \lesssim t \lesssim 53$, $\boldsymbol{u}^a(t)$ is confined to the part of the chaotic set (which we will refer to as lobe 2) that is centred at $\mathcal{H} = \mathcal{H}_2 \approx -0.003$. The chaotic set has several other lobes, as will be discussed shortly.

The relation between these lobes and ECSs can be seen in a low-dimensional projection of the state space onto $\mathcal{E}$, $\mathcal{D}$ and $\mathcal{H}$ shown in figure 3. The portions of turbulent trajectory $\boldsymbol{u}^a(t)$ confined to lobe 1 (lobe 2) are shown as a blue (red) cloud of points, representing different snapshots of the flow. For each ECS $\boldsymbol{u}_n$ that is not reflection symmetric, both $\boldsymbol{u}_n$ and $K_z\boldsymbol{u}_n$ are shown in figure 3. Since all three coordinates are invariant with respect to rotations around the axis, a family of temporally periodic solutions corresponding to each TW, i.e. $R_\phi\boldsymbol{u}_n$ with $\phi \in [0, 2\pi)$, is mapped to a single point. Similarly, a family of temporally quasi-periodic solutions corresponding to each RPO is mapped to a single closed curve. A large number of computed ECSs (TW_{01}, RPO_{01}–RPO_{12} and RPO_{19}) are collocated with lobe 1, as illustrated in figure 4(*a*), but we could not find any ECSs collocated with lobe 2. Instead, all initial conditions in lobe 2 converged to ECSs that lie outside of both lobes 1 and 2. Indeed, there is no guarantee that Newton iterations converge to a solution that is close to the near recurrence used as the corresponding initial condition. At first glance, this appears to suggest that some of the ECSs we found are dynamically relevant and some are not.

Interestingly, most of the ECSs lying outside of lobes 1 and 2 were found to be grouped in the same region of the state space. This grouping suggests that these solutions may be a part of the skeleton underlying a different lobe of the same chaotic set or, perhaps, a different chaotic set. In fact, by using an RPO lying in that region of the state space to initialize the flow, we computed a second turbulent trajectory, $\boldsymbol{u}^b(t)$, which remained confined to a region of the state space centred at $\mathcal{H} = \mathcal{H}_3 \approx -0.013$ for 60 time units. The corresponding running average of helicity is shown in red in figure 2 and snapshots of $\boldsymbol{u}^b(t)$ are shown as a green point cloud in figure 3. Here RPO_{13}–RPO_{18} and RPO_{20} as well as TW_{02} are collocated with this set, referred to as lobe 3 below, as figure 4(*b*) illustrates.

To determine whether lobe 3 is dynamically connected to lobes 1 and 2, we continued the turbulent trajectory $\boldsymbol{u}^a(t)$ further in time. The running average of helicity for a portion of this trajectory (we will refer to it as $\boldsymbol{u}^c(t)$) is shown in green in figure 2. It is clear

https://doi.org/10.1017/jfm.2021.522 Published online by Cambridge University Press

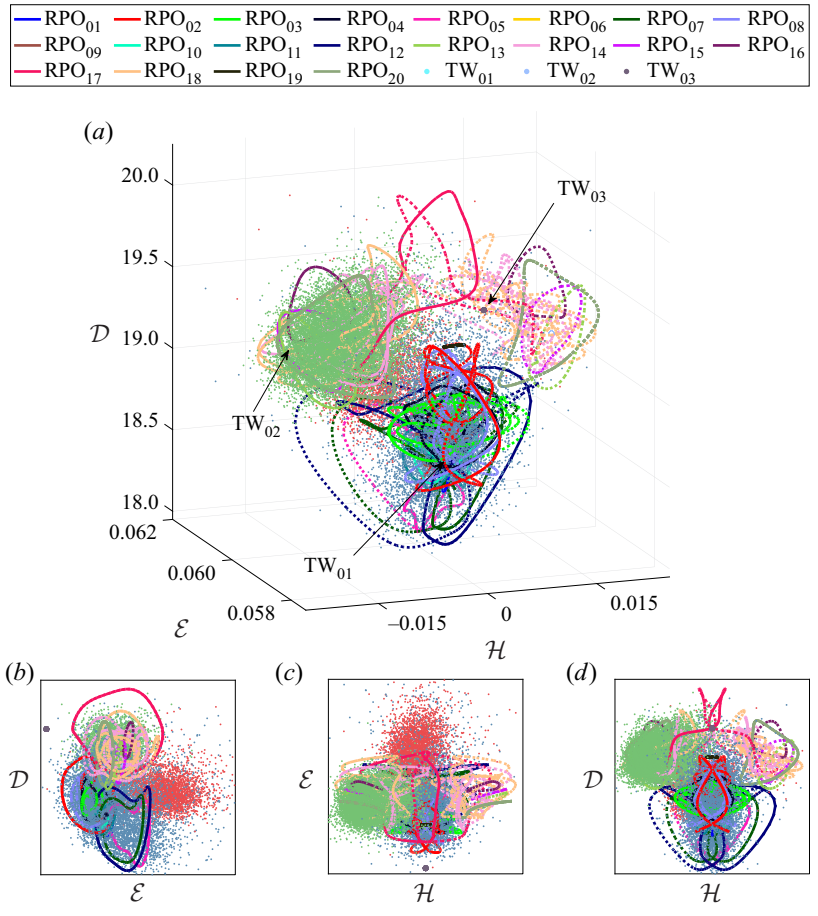


Figure 3. Three-dimensional projection of the infinite-dimensional state space (*a*) and the corresponding two-dimensional projections (*b–d*). The coordinates used are the energy $\mathcal{E}$, the rate of energy dissipation $\mathcal{D}$ and the helicity $\mathcal{H}$. The individual lobes of the chaotic set are shown as clouds of points with different colour: lobe 1 shown in blue; lobe 2 in red; lobe 3 in green. The computed RPOs (TWs) are shown as solid lines (filled circles) and their symmetry-related copies as dotted lines (open circles) of the same colour.

that this trajectory visits lobes 1 and 2 as well as the symmetric (under reflection K_z) copies of lobes 2 and 3. This suggests that lobe 1 as well as lobes 2 and 3 and their symmetric copies are all dynamically connected. The turbulent trajectory $\boldsymbol{u}^c(t)$ will not be analysed in the remainder of this paper. We will simply note that, after several hundred time units, turbulent flow eventually escapes the chaotic set composed of the five lobes mentioned previously and settles on what appears to be a stable quasiperiodic state. Hence, in our system, turbulence is a long-lived transient, similar to what was found in the same geometry at a larger aspect ratio (Hochstrate *et al.* 2010).

In the subsequent discussion, we will refer to the portion of $\boldsymbol{u}^a(t)$ restricted to lobes 1 and 2 of the chaotic set as $\boldsymbol{u}^1(t)$ and $\boldsymbol{u}^2(t)$, respectively. We will also identify $\boldsymbol{u}^3(t) = \boldsymbol{u}^b(t)$, since $\boldsymbol{u}^b(t)$ remains in lobe 3 for the entire interval over which it was computed. The characteristic flow fields in each lobe are compared in figure 5, where the velocity field associated with $\boldsymbol{u}^1(t)$, $\boldsymbol{u}^2(t)$ or $\boldsymbol{u}^3(t)$ has been averaged in both time and θ. Inside each lobe, we find two cellular vortical structures. In lobe 1, the two vortices are symmetric. In lobes

https://doi.org/10.1017/jfm.2021.522 Published online by Cambridge University Press

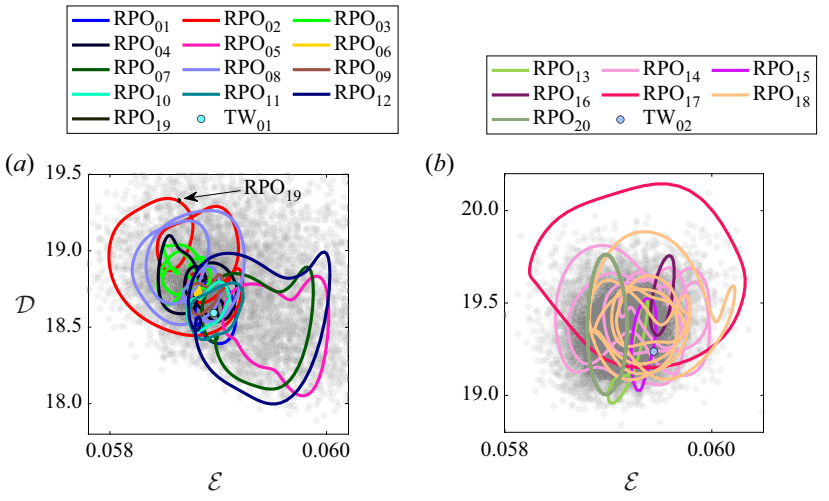


Figure 4. Two-dimensional projection of (*a*) lobe 1 and (*b*) lobe 3. In each lobe, the chaotic set (grey point cloud) is in the background. The RPOs and TWs collocated with each lobe in this projection are overlaid as solid curves and filled circles, respectively.

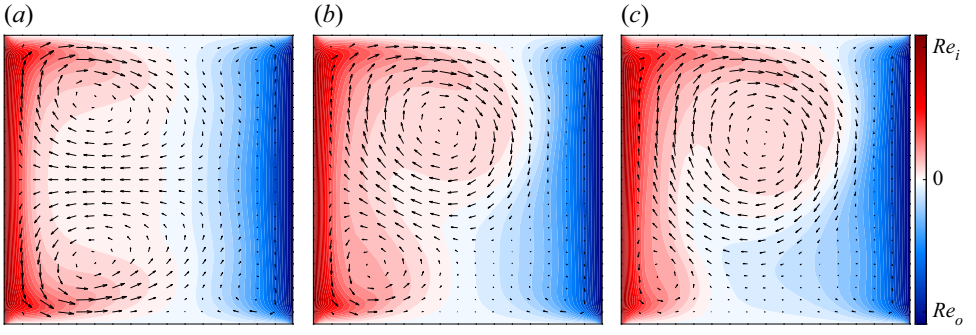


Figure 5. Mean flow field in (*a*) lobe 1, (*b*) lobe 2 and (*c*) lobe 3. In this figure and all following two-dimensional slices, the arrows show the in-plane (r and z) components of the flow and the colour indicates the out-of-plane (θ) component.

2 and 3, one vortex is notably stronger than the other. This asymmetric flow structure illustrates the reflection symmetry breaking and explains the relative arrangement of the three lobes along the $\mathcal{H}$ axis in figure 3.

At first glance, the spatial structure of the mean flow in different lobes appears to be similar to the structure of either single-cell (A1) or double-cell (N2) stationary cellular flows found for this (or similar) geometry in previous studies, which considered the case $Re_o = 0$ (Cliffe 1983; Pfister *et al.* 1988; Furukawa *et al.* 2002). Furthermore, N2 was found to be stable for $Re_i \lesssim 133$ and is replaced by A1 (or its symmetric copy) at a higher Re_i. The onset of time-dependence at $Re_i \approx 892$ does not appear to alter the structure of the flow dramatically (Marques & Lopéz 2006). Weak counter-rotation stabilizes symmetric flows (such as N2) at the expense of the asymmetric ones (such as A1), but does not notably modify the structure of the flows either (Schulz *et al.* 2003).

The set-up considered here leads to a (nearly) symmetric flow in lobe 1 that has one qualitative difference with N2: the sign of the azimuthal vorticity ω_θ is opposite to that

https://doi.org/10.1017/jfm.2021.522 Published online by Cambridge University Press

found in previous studies. In our case, the radial velocity is the largest and is positive near the end-caps, as figure 5(*a*) illustrates. For N2, the radial velocity is the largest and is positive at the centre plane $z = 0$; it represents a strong central jet of angular momentum (Marques & Lopéz 2006; Altmeyer *et al.* 2012) which is not found in lobe 1. These differences are likely due to our choice of the outer cylinder rotating independently of the end-caps; in previous studies of TCF, the end-caps were assumed to rotate with the same angular velocity as the outer cylinder.

3.2. *A measure of closeness*

Figure 3 suggests that most of the ECSs we found are embedded into either lobe 1 or lobe 3 of the chaotic set and, therefore, are dynamically relevant. However, low-dimensional projections can be misleading. To determine that an ECS is truly dynamically relevant, we need to ensure

(i) that turbulent flow comes close to an ECS, at least occasionally, in the full state space;
(ii) that turbulent flow remains in the neighbourhood of the ECS over a characteristic time scale of the flow; and
(iii) that turbulent flow shadows (i.e. evolves in a manner similar to) the ECS over time, while inside the neighbourhood of the ECS.

We will investigate whether these three conditions are satisfied in the remainder of the paper but, first, we need to define what 'close' means in either the physical space or the corresponding high-dimensional state space. The term ECS reflects the visual similarity between (spatial) structures commonly observed in a turbulent flow and snapshots of (numerically) exact solutions of Navier–Stokes in the three-dimensional physical space. Visual similarity is, however, too qualitative to be of much use for the purposes of predicting dynamics, even on relatively short time scales; we need a more quantitative definition of similarity.

Similarity is a relative term; before it is defined, we need to determine a yard stick for what is considered dissimilar. For parameters considered here, turbulent TCF $\boldsymbol{u}(t)$ is characterized by a fluctuation $\tilde{\boldsymbol{u}}(t) = \boldsymbol{u}(t) - \bar{\boldsymbol{u}}$ about an axially symmetric mean flow $\bar{\boldsymbol{u}} = \langle \boldsymbol{u}(t) \rangle_t$ that is small compared with this mean flow, i.e. $\|\tilde{\boldsymbol{u}}(t)\| \ll \|\bar{\boldsymbol{u}}\|$. Hence, the characteristic magnitude $\sigma = \langle \|\tilde{\boldsymbol{u}}(t)\| \rangle_t$ of the fluctuations about the mean flow – effectively the 'radius' of the chaotic set – is a more appropriate scale for the dissimilarity in the physical space, or distance in the state space, between different flow states than the magnitude $\|\bar{\boldsymbol{u}}\|$ of the mean flow.

Since dynamics partition the chaotic set into three different lobes, there are many different ways to define σ. To avoid ambiguity, we define it using a turbulent trajectory that lies entirely inside lobe 1. Fortunately, the diameters of all three lobes are quite similar. Next we define the (normalized) distance from an arbitrary point $\boldsymbol{u}$ in the state space to the family of solutions $R_\phi \boldsymbol{u}_n(\tau)$,

$$D_n(\boldsymbol{u}) = \min_{\phi,\tau} \sigma^{-1} \|\boldsymbol{u} - R_\phi \boldsymbol{u}_n(\tau)\|, \tag{3.4}$$

where τ defines the temporal phase along the RPO (this dependence is omitted for TWs for which time evolution is equivalent to rotation). The distance

$$D_n^j(t) = D_n(\boldsymbol{u}^j(t)) \tag{3.5}$$

https://doi.org/10.1017/jfm.2021.522 Published online by Cambridge University Press

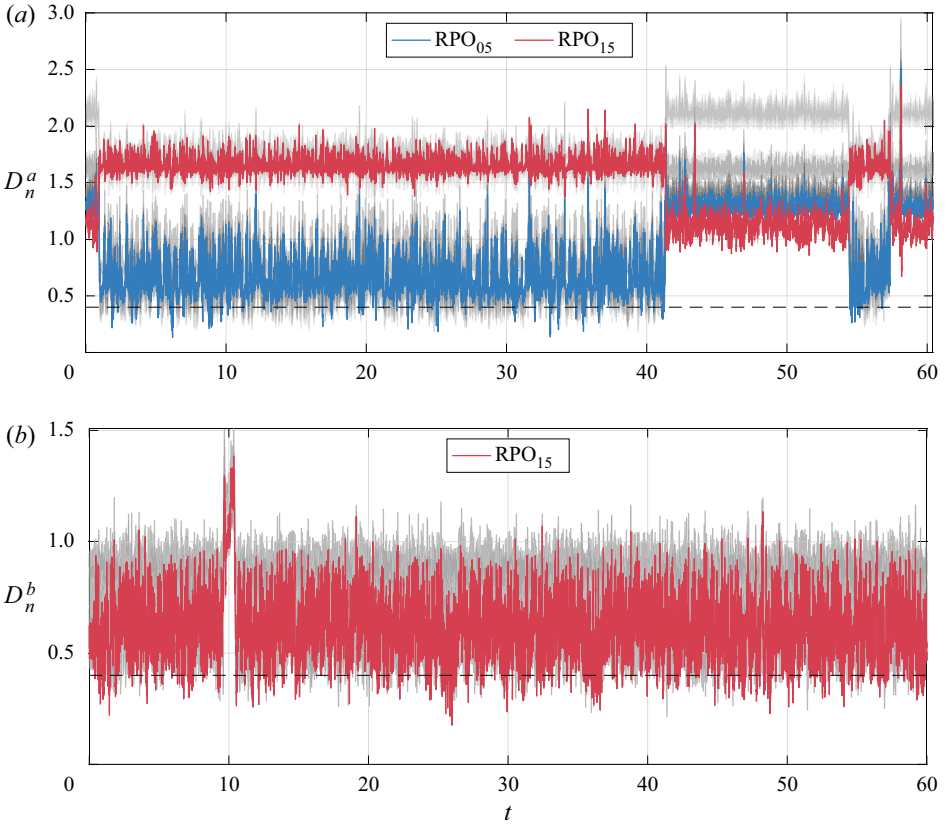


Figure 6. (*a*) The distance $D_n^a(t)$ between the turbulent trajectory $\boldsymbol{u}^a(t)$ confined to both lobes 1 and 2 and every ECS $\boldsymbol{u}_n$. All ECSs except for RPO_{05} and RPO_{15} are shown in grey. (*b*) The distance $D_n^b(t)$ between the turbulent trajectory $\boldsymbol{u}^b(t)$ inside lobe 3 and ECSs collocated with this lobe. All ECSs except for RPO_{15} are shown in grey. The dashed line indicates our chosen threshold $\bar{D}$ below which two states are considered 'close'.

measures how similar (close in the state space) the turbulent flow field snapshot $\boldsymbol{u}^j(t)$ is to the family of solutions $R_\phi \boldsymbol{u}_n(\tau)$. We will use $j = a, b$ when referring to the entire turbulent trajectories $\boldsymbol{u}^a(t)$ and $\boldsymbol{u}^b(t)$ and $j = 1, 2, 3$ when referring to the portion of those trajectories confined to lobes 1, 2 or 3. We will drop the indices when this does not cause confusion. The distances from both turbulent trajectories, $\boldsymbol{u}^a(t)$ and $\boldsymbol{u}^b(t)$, to various ECSs are shown in figure 6, with the minimal values listed in table 1. The lengths of both turbulent trajectories correspond to $O(10^4)$ periods of the shortest RPO we found, so they are likely long enough to sample a significant fraction of all three lobes.

Let us first consider the turbulent trajectory $\boldsymbol{u}^a(t)$ confined to lobes 1 and 2, which was used to generate the initial conditions for the Newton search. The distances to all the ECSs (as well as their symmetry-related copies) are shown in grey in figure 6(*a*), except for two solutions: RPO_{05} (in blue) and RPO_{15} (in red). All of the distances jump sharply at $t \approx 1$, 42, 54 and 57, as can be clearly seen by focusing on the distance to RPO_{05} and RPO_{15}, characterized, respectively, by a low (high) average value of $|\mathcal{H}|$. These jumps correspond to the turbulent trajectory moving between lobes 1 and 2. When the distance to RPO_{05} is low (high), the turbulent flow is inside lobe 1 (lobe 2). Recall that RPO_{15} lies inside lobe 3, which is closer to lobe 2, so the distance to this RPO shows the opposite trend.

https://doi.org/10.1017/jfm.2021.522 Published online by Cambridge University Press

Such behaviour is an example of intermittency, which is a characteristic feature of all turbulent flows, but is particularly apparent in transitional flows (Chaté & Manneville 1987) where it commonly manifests itself as spatiotemporal alternation between laminar and turbulent behaviour (Eckhardt *et al.* 2007). In the present case, intermittency represents a competition between different flow patterns shown in figure 5(*a*,*b*) – a phenomenon which has been observed in TCF at large Γ (Tsameret & Steinberg 1994) as well as in many other non-equilibrium systems.

Figure 6(*a*) shows that the turbulent trajectory $\boldsymbol{u}^a(t)$ spends most of the time in lobe 1 (e.g. for $1 \lesssim t \lesssim 42$). This is the likely reason most of the ECSs we found using a Newton search also lie in that lobe. Indeed, each of the fourteen ECSs (TW_{01}, RPO_{01}–RPO_{12} and RPO_{19}) that is collocated with lobe 1 in the projection shown in figure 3 was also found to be collocated with this lobe in the full state space, with $D_n^1(t) \approx 0.6$ on average (and a minimum of around 0.2) during the intervals when the turbulent flow is inside lobe 1.

The situation is similar for the turbulent trajectory $\boldsymbol{u}^b(t)$ confined to lobe 3. For the eight ECSs collocated with this lobe in the low-dimensional projection (TW_{02}, RPO_{13}–RPO_{18} and RPO_{20}), the distance is $D_n^3(t) \approx 0.7$ on average and gets as low as 0.3 or so, according to figure 6(*b*). The spike around $t = 10$ appears to represent an 'extreme' event, where the turbulent trajectory explores the periphery of lobe 3. The discussion in the remainder of the paper will focus mainly on lobe 1, which contains most of the ECSs found.

To get a sense of the relationship between the magnitude of the distance in the state space and the similarity of the flow fields in the physical space, we compare snapshots of the turbulent flow field $\boldsymbol{u}^a(t)$ with a nearby ECS for various values of $D(t)$ in figure 7. The flow fields appear visually similar for $D(t) \lesssim \bar{D}$ with $\bar{D} = 0.4$, while for $D(t) \gtrsim \bar{D}$ the differences become apparent. Based on this comparison, we define two flow states to be similar (dissimilar), or close (far) in the state space, for $D(t) < \bar{D}$ ($D(t) > \bar{D}$). The corresponding threshold $\bar{D}$ is shown as the dashed horizontal lines in figure 6. While using such an 'ocular norm' to define closeness of different flow states may appear somewhat arbitrary, it is quite common in analysing experimental data (De Lozar *et al.* 2012).

Instead of relying on a somewhat subjective metric based on qualitative similarity of different flow fields, the distance threshold can be chosen based on a partition of the chaotic set induced by the set of computed ECSs. Let us partition lobe 1 into tubular neighbourhoods of different ECSs with sizes determined by $\bar{D}$. To get a sense of how large a fraction of lobe 1 is covered by the union of these neighbourhoods, we computed the probability P that turbulent flow $\boldsymbol{u}^a(t)$, restricted to lobe 1, is in the neighbourhood of any of the fourteen ECSs collocated with this lobe. As figure 8(*b*) illustrates, these neighbourhoods cover nearly 100 % of lobe 1 for $\bar{D} \gtrsim 1$, approximately 40 % for $\bar{D} = 0.4$, and less than 1 % for $\bar{D} \lesssim 0.2$.

Alternatively, $\bar{D}$ can be chosen based on the separation between different ECSs. At small $\bar{D}$, their neighbourhoods will not overlap. As $\bar{D}$ is increased, different neighbourhoods start to overlap more and more. As figure 8(*a*) shows, the minimal distance

$$D_{nk}^{min} = \min_{\phi,t,\tau} \sigma^{-1} \|\boldsymbol{u}_k(t) - R_\phi \boldsymbol{u}_n(\tau)\|, \tag{3.6}$$

between pairs of ECSs is typically around 0.4 or larger, so our choice of $\bar{D}$ should be sufficient to distinguish different ECSs. The minimal distance between some pairs of ECSs (e.g. RPO_{09}–RPO_{11}), however, is as low as 0.2, which means that individual snapshots of these solutions may not be visually distinct.

The results presented in this section show that a snapshot of turbulent flow $\boldsymbol{u}^j(t)$ is close to a family of ECSs $R_\phi \boldsymbol{u}_n$ provided $D_n^j(t) < \bar{D}$, where $\bar{D} = 0.4$. As figure 6(*a*) illustrates,

https://doi.org/10.1017/jfm.2021.522 Published online by Cambridge University Press

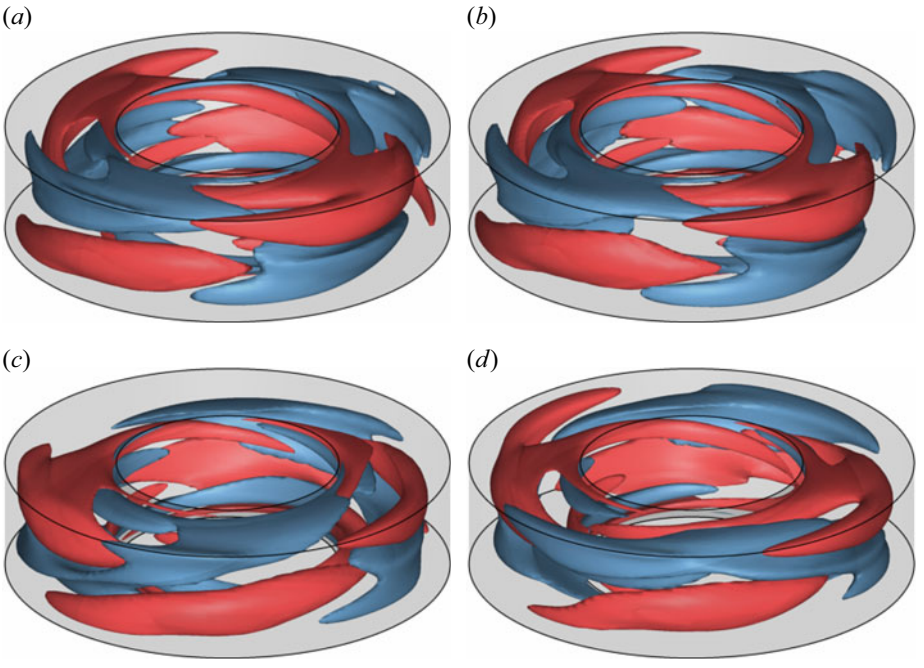


Figure 7. Comparison of (*a*) the turbulent flow field $\boldsymbol{u}^a(t)$ and (*b*) RPO_{04} at an instant where $D^a_7(t) = 0.34$ is below threshold. Comparison of (*c*) the turbulent flow field $\boldsymbol{u}^a(t)$ and (*d*) RPO_{12} at an instant where $D^a_{15}(t) = 0.78$ is above threshold. To represent the flow structure in the entire flow domain, here and below, we show two level sets of u_θ, one with a positive value (in red) and one with a negative value (in blue). In all plots, the mean flow has been subtracted off.

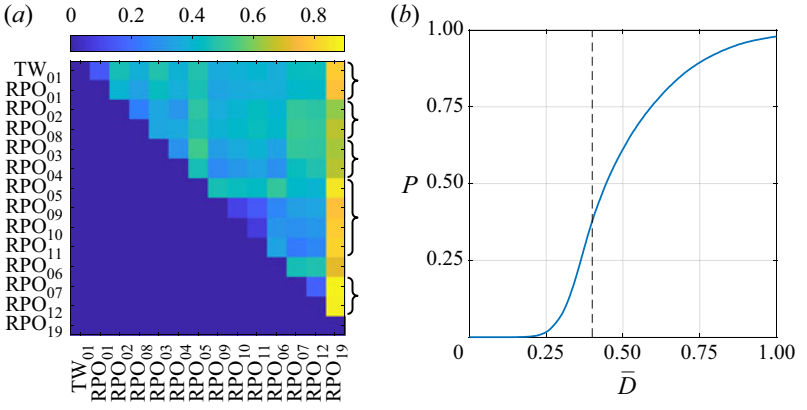


Figure 8. (*a*) The minimal distance, D^{min}_{nk}, between RPOs collocated with lobe 1. Braces on the right of the panel group together RPOs that are connected by continuation in Re_i. (*b*) The probability that a snapshot of the turbulent trajectory will lie in a neighbourhood of the ECS shown in panel (*a*), as a function of tubular neighbourhood radius, $\bar{D}$. The dashed line indicates our chosen threshold below which two states are considered 'close'.

the turbulent trajectory $\boldsymbol{u}^a(t)$ comes close to multiple RPOs and one TW collocated with lobe 1; this happens quite frequently. Similarly, figure 6(*b*) illustrates that turbulent trajectory $\boldsymbol{u}^b(t)$ comes close to multiple RPOs and one TW collocated with lobe 3. In particular we find that condition (i) for dynamical relevance is satisfied for all ECSs

https://doi.org/10.1017/jfm.2021.522 Published online by Cambridge University Press

collocated with lobe 1, with the possible exception of RPO_{19} (cf. table 1). Figure 8(*a*) shows that RPO_{19} lies far from all other solutions collocated with lobe 1. This suggests that TW_{01} and RPO_{01}–RPO_{12} are actually embedded in the primary lobe and may play a dynamically important role, while RPO_{19} does not.

3.3. *Shadowing of solutions*

Next we turn to checking conditions (ii) and (iii) of dynamical relevance using time intervals where $D_n^j(t) < \bar{D}$ for a given n. While condition (ii) is easy to verify by direct inspection, verifying shadowing condition (iii) requires more care. Formally, shadowing is defined for chaotic trajectories that come infinitesimally close to an unstable solution (Gaspard 2005). In our case, none of the computed ECS families are approached particularly closely by turbulent flow on time scales accessible to numerical simulations or experiments. One, therefore, has to define shadowing in practically meaningful terms. Yalnız *et al.* (2020) proposed a topological approach to define shadowing of UPOs in a turbulent flow confined to a subspace with only discrete symmetries. The approach is based on computing the number of connected components and holes for temporally discretized trajectories over one temporal period of the solution and comparing the corresponding persistence diagrams using the bottleneck distance. We define shadowing events differently for several reasons. First of all, the period of an ECS is not a proper time scale: in practice, ECSs with longer periods will never be shadowed fully. Instead, an ECS $\boldsymbol{u}_n$ will typically be shadowed for an interval of time comparable to the inverse of the escape rate

$$\gamma_n = \sum_k \lambda_{n,k}, \tag{3.7}$$

where the sum goes over the unstable directions associated with the ECS and $\lambda_{n,k}$ are the corresponding Floquet exponents. We only require an ECS to be shadowed for an interval equal to its expected escape time γ_n^{-1}. The mean escape times are 0.024 for lobe 1 and 0.006 for lobe 3.

Furthermore, the approach used here is both less complicated and allows one to define shadowing for both RPOs and TWs. It is essentially a generalization of the approach proposed by Suri *et al.* (2020) for UPOs and relies on the skew product decomposition of the dynamics (Fiedler *et al.* 1996; Sandstede, Scheel & Wulff 1999) in the vicinity of relative solutions induced by continuous symmetries. For each RPO, the computed ECS $\boldsymbol{u}_n(\tau)$ represents a family of solutions that lie on a two-torus in the state space; all points of this two-torus can be parameterised as $R_\phi \boldsymbol{u}_n(\tau)$, where $0 < \phi < 2\pi/N$ and $0 < \tau < T$. Let $R_\phi \boldsymbol{u}_n(\tau)$ be a point in the family of solutions that is closest to a point $\boldsymbol{u}^a(t)$ on the turbulent trajectory, such that

$$\{\tau(t), \phi(t)\} = \arg\min_{\tau,\phi} \sigma^{-1} \|\boldsymbol{u}^a(t) - R_\phi \boldsymbol{u}_n(\tau)\|, \tag{3.8}$$

where ϕ is constrained to the interval $[0, 2\pi/N)$ for solutions with an N-fold discrete rotational symmetry (e.g. $N = 2$ for RPO_{01} and RPO_{15}). In this decomposition, coordinates τ and ϕ describe the evolution along the group manifold (time translations and rotations), while D_n^a describes the evolution transverse to the group manifold. Below, we will drop the subscript and superscript of D since the context makes it clear which turbulent solution and ECS is discussed.

For $D = 0$, a trajectory $\boldsymbol{u}(t)$ will have $\mathrm{d}\tau/\mathrm{d}t = 1$ and $\mathrm{d}\phi/\mathrm{d}t = 0$ for $0 < \tau < T$. Once per period, both $\tau(t)$ and $\phi(t)$ will experience a jump by, respectively, T and Φ

https://doi.org/10.1017/jfm.2021.522 Published online by Cambridge University Press

(see table 1). The discontinuities in $\tau(t)$ and $\phi(t)$ can be removed using coordinates $\tilde{\tau}$ and $\tilde{\phi}$ such that

$$\left.\begin{aligned}\tau &= \tilde{\tau} \bmod T,\\ \tilde{\phi} &= \phi \bmod \Phi.\end{aligned}\right\} \tag{3.9}$$

Then, for $D = 0$, $\mathrm{d}\tilde{\tau}/\mathrm{d}t = 1$ and $\mathrm{d}\tilde{\phi}/\mathrm{d}t = 0$ for all t. For any trajectory that has a small but non-zero D, the dynamics of τ and ϕ should be qualitatively similar: $\mathrm{d}\tilde{\tau}/\mathrm{d}t \approx 1$ and $\mathrm{d}\tilde{\phi}/\mathrm{d}t \approx 0$. The evolution of D, τ and ϕ can therefore be used to define a set of natural criteria for shadowing of an RPO.

Specifically, we will consider a turbulent trajectory to shadow an RPO if, for a temporal interval $I(t) = [t - \gamma_n^{-1}/2, t + \gamma_n^{-1}/2]$, all three coordinates evolve similarly to the way they would for the RPO. In practice, we define similarity in terms of normalized deviations

$$\left.\begin{aligned}E_\tau &= \min_{t_0} \frac{1}{T\gamma_n^{-1}} \int_{I(t)} |t' + t_0 - \tilde{\tau}(t')|^2 \,\mathrm{d}t'\\ E_\phi &= \min_{\phi_0} \frac{N}{\pi\gamma_n^{-1}} \int_{I(t)} |\phi_0 - \tilde{\phi}(t')|^2 \,\mathrm{d}t'\end{aligned}\right\} \tag{3.10}$$

of $\tilde{\tau}$ and $\tilde{\phi}$ from straight lines with slope one and zero, respectively. The turbulent trajectory is considered to be shadowing an RPO, if the following three conditions are satisfied:

(a) $D(t') < \bar{D}$ for $t' \in I(t)$;
(b) $E_\tau < \bar{E}_\tau$; and
(c) $E_\phi < \bar{E}_\phi$

for an appropriate choice of the thresholds $\bar{E}_\tau$ and $\bar{E}_\phi$. For TWs, the two coordinates describing the evolution along the group manifold are not independent, $\mathrm{d}\tau/\mathrm{d}\phi = T/\Phi$. In this case, shadowing is determined by two of the three conditions, (a) and (b).

We chose $\bar{E}_\tau = 0.0001$ and $\bar{E}_\phi = 0.0003$, so that conditions (a–c) are satisfied with roughly equal probability. Figure 9 summarizes the results for both the turbulent trajectory $\boldsymbol{u}^a(t)$ confined to lobes 1 and 2 and the turbulent trajectory $\boldsymbol{u}^b(t)$ confined to lobe 3. In the former case, we find that turbulence shadows both RPOs and a TW. Moreover, if an ECS is shadowed, then so is its reflected copy. This suggests that turbulence does not break reflection symmetry in a statistical sense, i.e. the probability of shadowing any ECS is comparable to the probability of shadowing its reflected copy. As figure 3 illustrates, this is not entirely unexpected, since lobe 1 is fairly symmetric with respect to the reflection.

For instance, consider a shadowing event for RPO_{05} shown in figure 10 and its symmetry-related copy in figure 11 (the corresponding movies are included as supplementary material). The same format is used here and below to illustrate shadowing events. Panel (*a*) shows the evolution of the three coordinates τ, $\tilde{\phi}$ and D with black (white) circles indicating instances when the corresponding shadowing criterion is satisfied (not satisfied). Red lines denote the temporal intervals when the criterion based on the corresponding coordinate is satisfied; for an interval to be considered an instance of shadowing, all three criteria must be met simultaneously. The grey bar shows the length of the interval γ_n^{-1} for comparison with the temporal period of the ECS. Panels (*b*) and (*c*) compare, respectively, the spatial structure (contours of constant u_θ at the values denoted in yellow on the colourbar in panels (*d*,*e*)) of the turbulent flow and the corresponding ECS in the entire domain at the instant denoted by the vertical black line in panel (*a*).

https://doi.org/10.1017/jfm.2021.522 Published online by Cambridge University Press

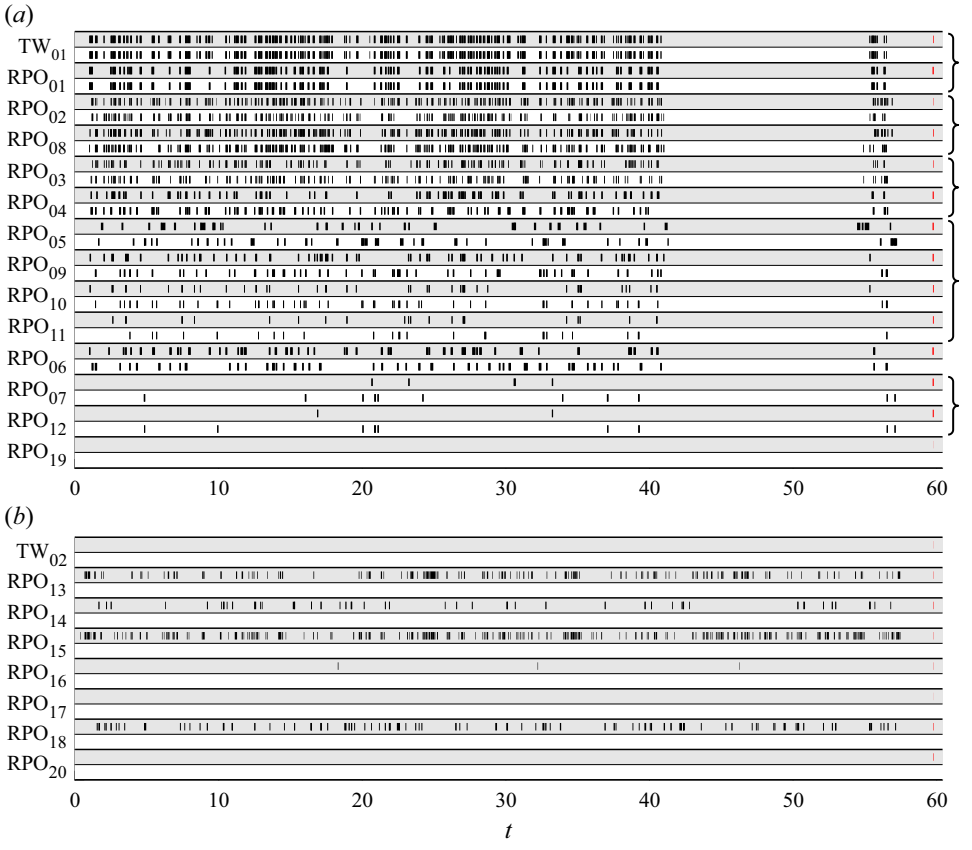


Figure 9. A summary of the shadowing events (marked with black bars) for each of the two turbulent trajectories, (*a*) $\boldsymbol{u}^a(t)$ and (*b*) $\boldsymbol{u}^b(t)$. Each ECS is represented by two rows, one for the numerically converged solution $\boldsymbol{u}_n$ (grey) and one for its symmetric copy $K_z\boldsymbol{u}_n$ (white). Red bars on the right represent the escape times γ_n^{-1} to scale. Curly braces on the far right group together RPOs that are related via continuation in Re_i.

Finally, panels (*d*) and (*e*) compare the velocity fields in the yellow cross-section shown in panels (*b*) and (*c*), respectively. In all panels, the turbulent mean flow is subtracted off.

Note that, for both RPO_{05} and its symmetry-related copy, the respective RPO is shadowed continuously for several periods (interval of around $6\gamma_n^{-1}$). During the shadowing intervals, all three criteria are satisfied to a high accuracy: the slope of $\tau(t)$ is near unity, the slope of $\tilde{\phi}(t)$ is near zero and $D(t)$ stays below the threshold $\bar{D}$. As discussed previously, for $D(t) < \bar{D}$ the turbulent flow is visually almost indistinguishable from the corresponding ECS in the entire domain. Figure 10(*b*,*c*) illustrates this particularly convincingly for RPO_{05}. The similarity is not just qualitative, but quantitative, as figure 10(*d*,*e*) shows. For small $D(t)$, it is expected that the turbulent flow evolves in the same manner as the nearby RPO. However, when $D(t)$ briefly increases above threshold, the slopes of $\tau(t)$ and $\tilde{\phi}(t)$ remain virtually unchanged, suggesting that turbulence continues shadowing the same member of the RPO family even when the corresponding flows are not very similar. Analogous statements apply to the reflected version of RPO_{05}, as figure 11 illustrates.

Figure 12 presents a sequence of several shadowing events for RPO_{01}. These shadowing events are of duration comparable to those for RPO_{05} and its reflection, measured in units

https://doi.org/10.1017/jfm.2021.522 Published online by Cambridge University Press

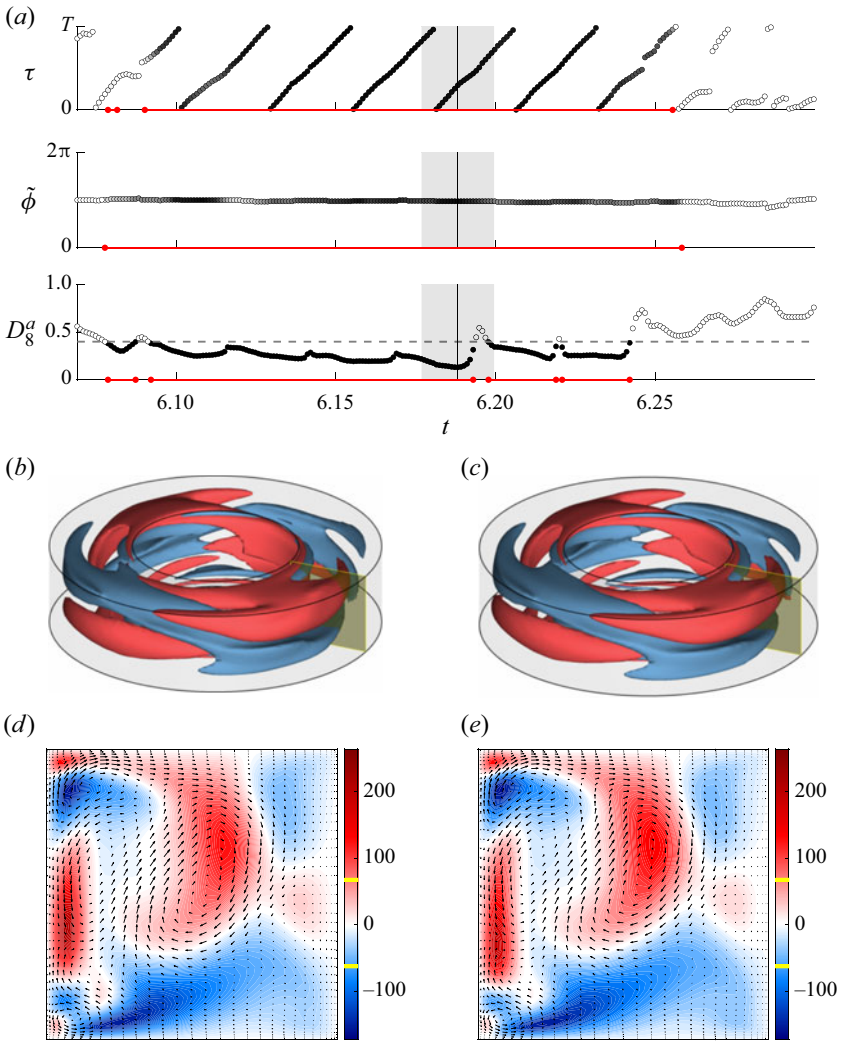


Figure 10. Turbulent flow $\boldsymbol{u}^a(t)$ shadowing RPO_{05}. (*a*) Evolution of coordinates τ, $\tilde{\phi}$ and D. Black (white) circles indicate instances when the corresponding shadowing criterion is satisfied (not satisfied). Red lines denote the temporal intervals during which a given criterion is satisfied. The grey bar shows the escape time, γ_n^{-1}. Snapshots of (*b*) the turbulent flow and (*c*) the ECS at the instant marked with the black vertical line in panel (*a*). Flow fields in the yellow cross-section for (*d*) the turbulent flow and (*e*) the ECS. A movie of this shadowing event is included as supplementary material available at https://doi.org/10.1017/jfm.2021.522.

of γ_n^{-1}, but correspond to quite a few periods of RPO_{01}. Not only that, turbulence also visits the neighbourhood of RPO_{01} much more frequently, as figure 9(*a*) demonstrates. In fact, this solution is by far the most frequently visited RPO in lobe 1. Note that RPO_{01} is symmetric with respect to $K_z R_{\pi/2}$, so reflection is equivalent to a rotation by $\pi/2$. Hence, both RPO_{01} and its reflection belong to the same solution family, and both rows in figure 9(*a*) contain identical sequences of shadowing events. Also, just like in the case of RPO_{05}, turbulent flow is essentially indistinguishable from RPO_{01} during the shadowing episodes.

Figure 13 illustrates shadowing of TW_{01}. Rather unexpectedly, TW_{01} is found to be shadowed even more frequently than RPO_{01}. In fact, when turbulent trajectory $\boldsymbol{u}^a(t)$ is

https://doi.org/10.1017/jfm.2021.522 Published online by Cambridge University Press

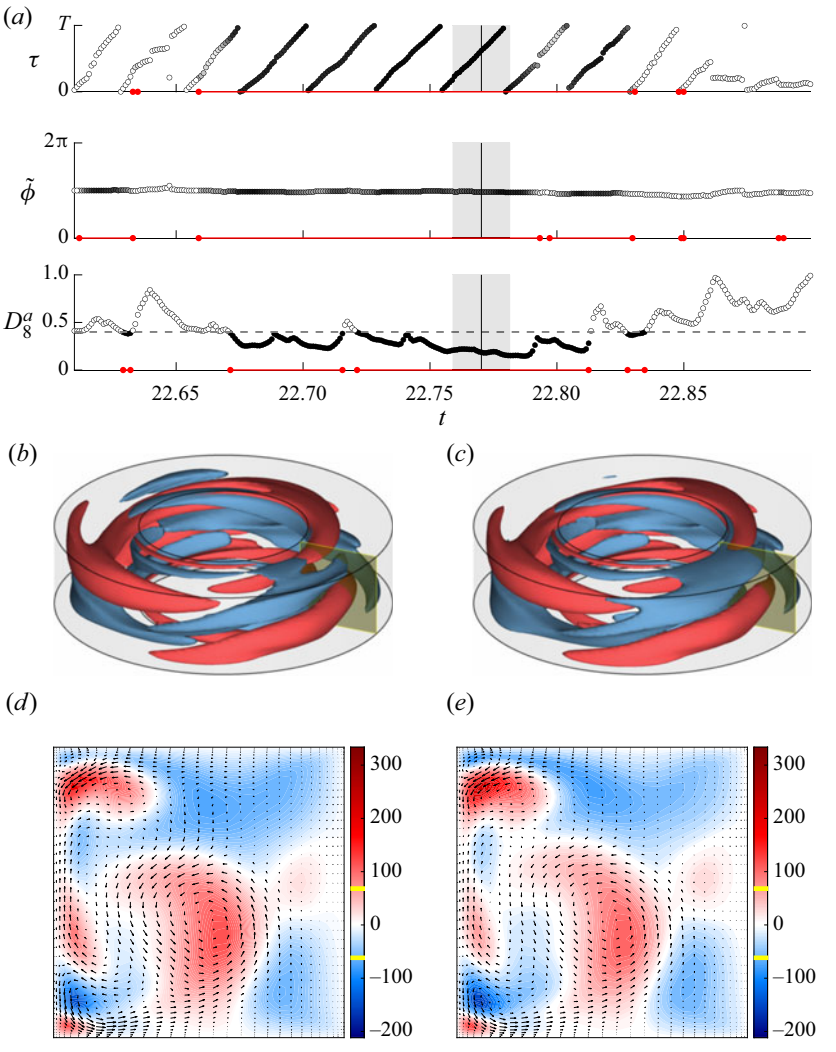


Figure 11. A shadowing event for the reflected copy of RPO_{05} in lobe 1. A corresponding movie is available as supplementary material.

inside lobe 1, it spends more time near TW_{01} than any other ECS according to figure 9(*a*). Moreover, when TW_{01} is shadowed, then typically so is RPO_{01}. This is not particularly surprising, as RPO_{01} is rather compact, and the two ECSs lie very close to each other, with the distance between them being roughly a half of $\bar{D}$ according to figure 8(*a*). This is a consequence of RPO_{01} being born in a Hopf bifurcation of TW_{01}, which happens to lie close in the parameter space. It should also be mentioned that the length of the shadowing intervals for TW_{01} tends to be quite large (e.g. around $8\gamma_n^{-1}$ for the event shown in figure 13) compared with typical shadowing intervals for the RPOs embedded in lobe 1.

We have not found any shadowing events for RPO_{19} or its reflection, even though it appears to be embedded inside lobe 1. Indeed, the smallest value of $D(t)$ for this ECS is 0.42, which is above our threshold $\bar{D}$. Every other RPO (as well as TW_{01}) embedded in lobe 1 is being shadowed by turbulence. Recall that $\boldsymbol{u}^a(t)$ visits both lobes 1 and 2. As expected, shadowing events are confined to the temporal intervals when turbulent flow is

https://doi.org/10.1017/jfm.2021.522 Published online by Cambridge University Press

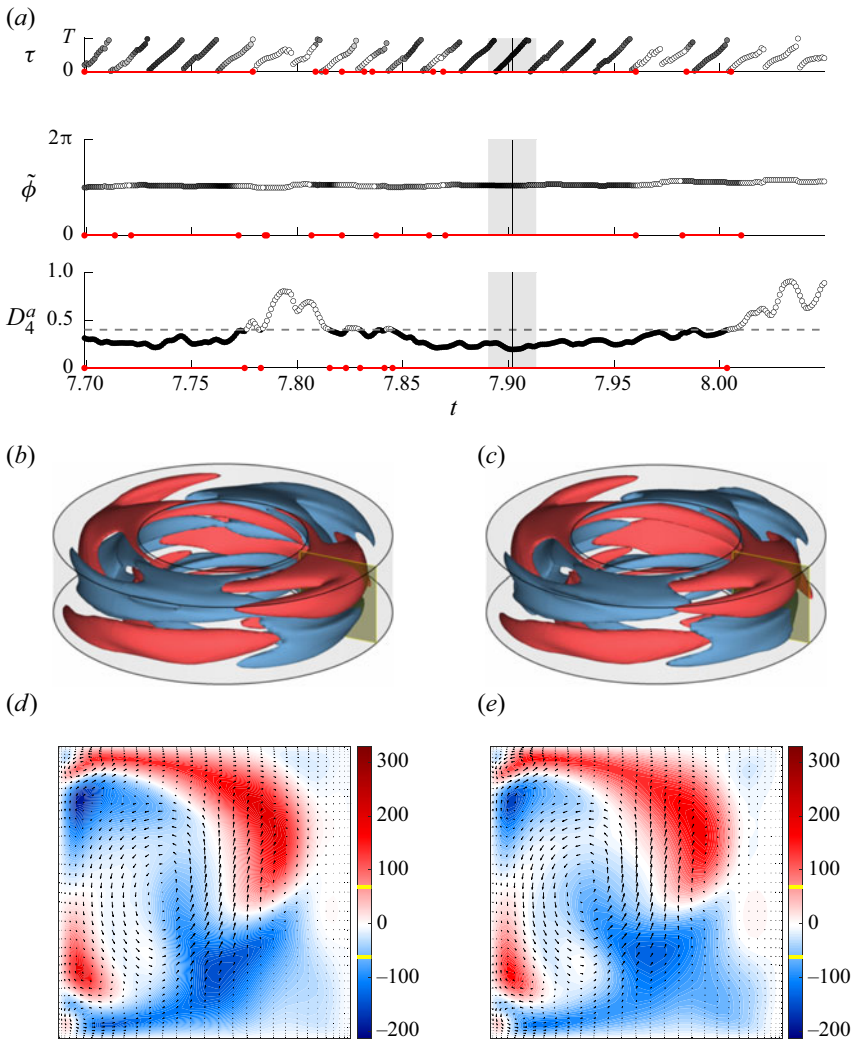


Figure 12. A shadowing event for RPO_{01} in lobe 1. A corresponding movie is available as supplementary material.

inside lobe 1. The shadowing criteria (*a–c*) are not satisfied when the turbulent trajectory is inside lobe 2 as we have not identified ECSs in that region of the state space.

For completeness, we have also performed a similar analysis for the turbulent trajectory $\boldsymbol{u}^b(t)$ which lies in lobe 3. It was found to shadow RPO_{13}–RPO_{16} and RPO_{18}. Since this lobe breaks the reflection symmetry, none of the reflected copies of these RPOs were shadowed. An example of shadowing for RPO_{15} is shown in figure 14. It is worth emphasizing that ECSs in lobe 3 are more unstable than those in lobe 1, as illustrated by both the larger number of unstable directions and the shorter escape time. As a result, there are fewer instances of shadowing and each shadowing event is nominally shorter. For instance, even though RPO_{15} is shadowed for almost three (very short) periods in figure 14, this interval corresponds to only 0.022 in non-dimensional units, compared with around 0.1 for RPO_{01} and RPO_{05}.

https://doi.org/10.1017/jfm.2021.522 Published online by Cambridge University Press

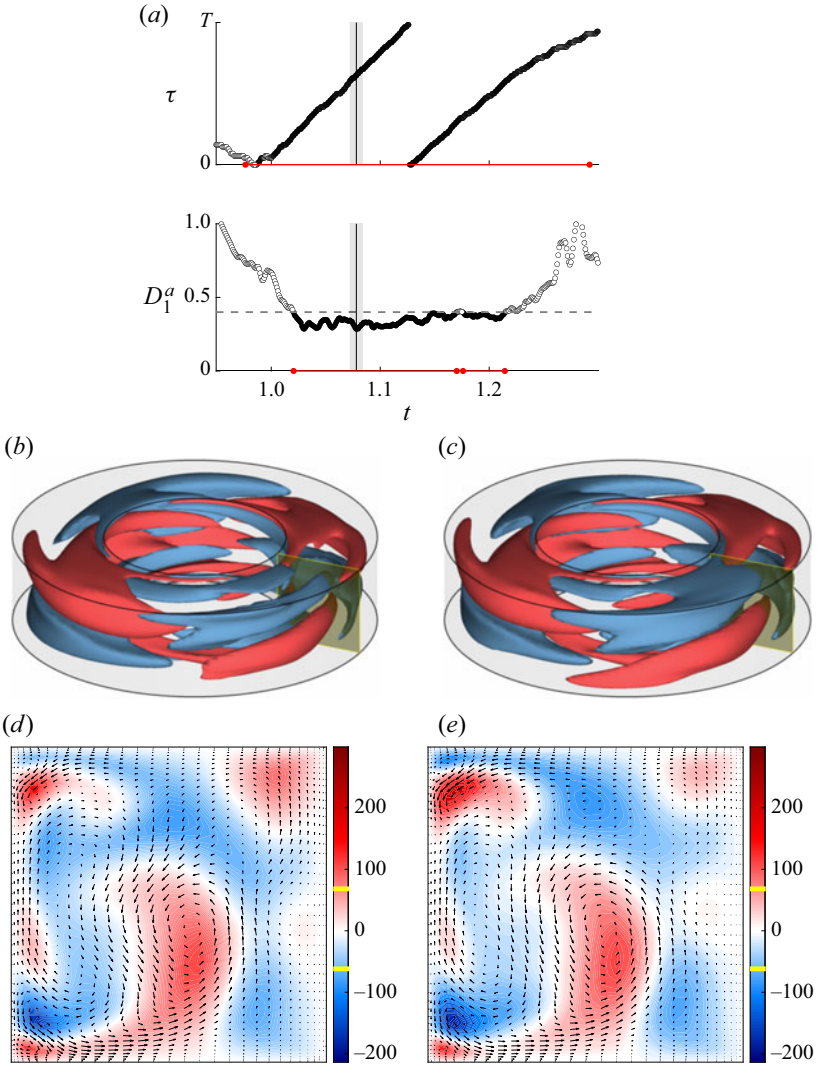


Figure 13. A shadowing event for TW_{01} in lobe 1. A corresponding movie is available as supplementary material.

4. Discussion

We have considered a new regime of small-aspect-ratio TCF where the two cylinders rotate in opposite directions, so both centrifugal and shear instabilities may induce and sustain turbulent flows. For the Reynolds numbers considered, we find that turbulent flows explore several distinct regions of the state space. These regions correspond to five lobes of the associated chaotic set that are dynamically connected to each other.

Discovery of lobe 3 was prompted by the observation that a large number of ECSs were found in the same region of the state space outside of lobes 1 and 2. While it is expected to find clusters of ECSs in regions of the state space inhabited by turbulence, to the best of our knowledge, this is the first example where a cluster of ECSs was found to predict the presence of a chaotic set supporting turbulent flow. The ECSs inside lobe 3 were found using both parameter continuation of ECSs inside lobe 1 and using a Newton–Krylov

https://doi.org/10.1017/jfm.2021.522 Published online by Cambridge University Press

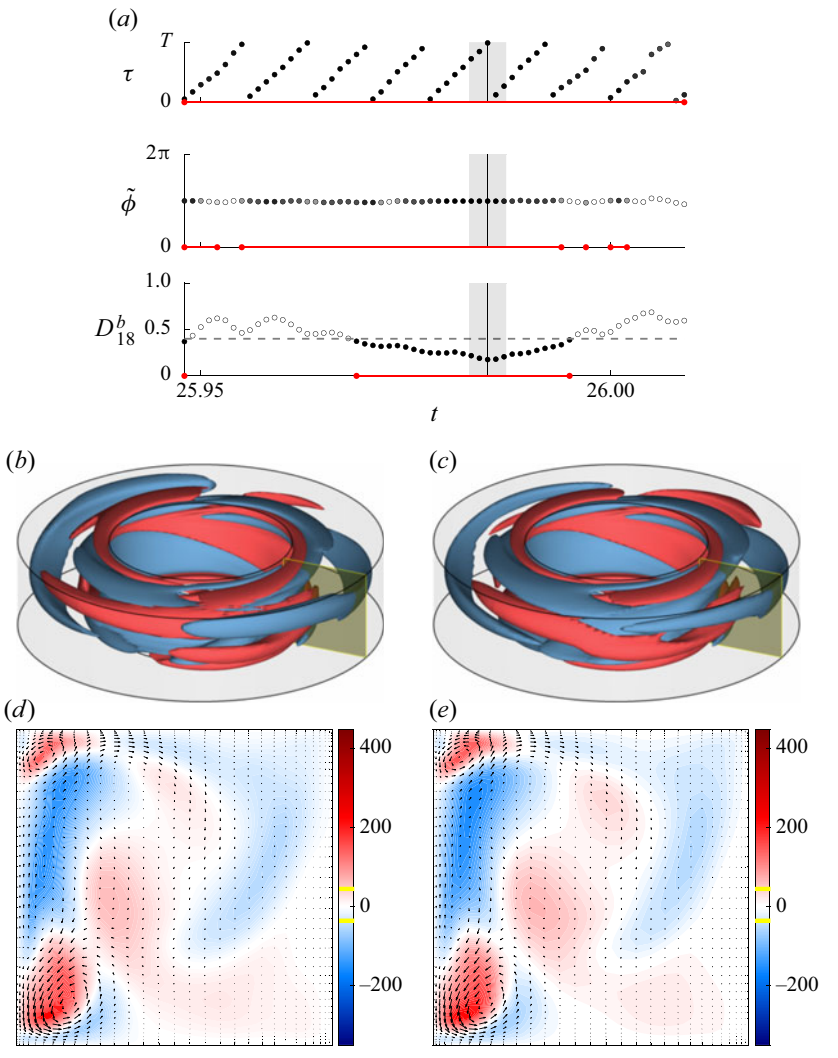


Figure 14. A shadowing event for RPO_{15} in lobe 3. A corresponding movie is available as supplementary material.

solver with initial conditions confined to lobe 1. This suggests that computation of large sets of ECSs is a fairly robust way of identifying initial conditions that lead to turbulence, at least of transient variety.

The majority of the computed ECSs were found to be collocated with either lobe 1 or lobe 3. Somewhat surprisingly, none of the ECSs were found to be collocated with lobe 2, although this may be due to the initial conditions for the Newton–Krylov solver lying mostly in lobe 1. Furthermore, some of the ECSs (e.g. TW_{03} computed via continuation) were found to lie outside of all three lobes of the chaotic set, which is not entirely surprising. Of the ECSs collocated with one of the lobes, the majority are RPOs, although TW_{01} and TW_{02} are also collocated with lobes 1 and 3, respectively. More importantly, most of the ECSs collocated with one or the other lobe are found to be shadowed by turbulent trajectories. A similar result appears to also hold for turbulent pipe flow, although

https://doi.org/10.1017/jfm.2021.522 Published online by Cambridge University Press

the respective study (Budanur *et al.* 2017) has only verified condition (*a*) for shadowing of a single RPO.

Closeness and shadowing are often assumed to be synonymous in the literature, which has fostered confusion in the field. In fact, it is possible for the turbulent trajectory to be close to an ECS and not shadow it. In particular, closeness implies that D is small regardless of whether the two solutions coevolve. On the other hand, shadowing implies coevolution, not just closeness, so that the ECS describes the dynamics of turbulent flow over some period of time. Hence, shadowing of an ECS implies that the ECS is dynamically relevant, while closeness to an ECS does not. Of course, for infinitesimally small D, closeness and shadowing do become equivalent. However, in practice turbulence never approaches any ECS infinitesimally closely. Our results suggest that Euclidean distance D between turbulent flow and an ECS family becoming small compared with its mean value is neither a necessary nor a sufficient condition for coevolution. As figures 10–12 illustrate, one routinely finds coevolution in terms of variables τ and ϕ parameterizing the group manifold, (i.e. conditions (*b*,*c*) being satisfied) for values of D that are not particularly small. Similarly, small values of D do not guarantee that τ and ϕ evolve as they should when turbulence shadows an RPO. Nonetheless, there is a strong correlation between the three conditions (*a*–*c*): when one is satisfied, more often than not so are the other two.

More importantly, given that D never becomes particularly small, we find many convincing examples of shadowing for both RPOs and TWs on accessible time scales, despite our library of ECSs being relatively small. This is critical for the practical utility of an ECS-based framework for a dynamical description of turbulent flow. If the computed ECSs were rarely shadowed by turbulence, that would imply a serious problem with this framework, indicating that dynamically important solutions have not been found and possibly do not even correspond to either RPOs or TWs. Admittedly, it is quite possible that (relative) quasi-periodic solutions may be more dynamically relevant than, say, the periodic ones. Of course, such a possibility cannot be excluded based on our results. Indeed, even for lobe 1, the neighbourhoods of a dozen or so embedded RPOs and TWs (plus their reflections), cover less than a half of this lobe, despite their relatively generous size, as illustrated in figure 8(*b*).

On the other hand, we found that multiple solutions may be shadowed simultaneously. As figure 9 illustrates, TW_{01} and RPO_{01} are frequently shadowed at the same time. The same is true of RPO_{02} and RPO_{08} or RPO_{07} and RPO_{12}. This is not coincidental as the respective solutions are themselves close. For instance, RPO_{07} and RPO_{12} shadow each other for their entire duration, as illustrated by a movie provided in the supplementary material. Close solutions are all related via parameter continuation; groups of related solutions are indicated with brackets in figures 8(*a*) and 9(*a*). For uniformly hyperbolic systems where periodic orbits are dense (Gaspard 2005), simultaneous shadowing of multiple unstable solutions is expected. The chaotic set underlying turbulence is not uniformly hyperbolic, as explained below. Despite this breakdown of uniform hyperbolicity, we find some RPOs to lie close enough to be shadowed simultaneously.

Unexpectedly, we found that the ECS that is shadowed the most by turbulent flow is a TW, not an RPO. This result is potentially quite significant, as it suggests that an extension of periodic orbit theory to systems with continuous symmetries may have to include contributions from solutions other than RPOs. Since turbulence spends a large fraction of time in the neighbourhood of TW_{01}, excluding the contribution from this ECS to the average of any observable would greatly impact the corresponding temporal mean.

https://doi.org/10.1017/jfm.2021.522 Published online by Cambridge University Press

Of course, it is possible that it is RPO_{01}, rather than TW_{01}, that plays the important dynamical and statistic role, with TW_{01} being shadowed because RPO_{01} is. Nonetheless, we chose a set of parameters that happens to be close to the bifurcation where RPO_{01} is born. As a result, RPO_{01} and TW_{01} are not very distinct. A similar analysis to ours would have to be repeated farther away from the bifurcation (e.g. at a higher Re_i) to determine which solution plays a more important role.

Finally, we find that the shadowing property is robust to small changes in system parameters. As many of the solutions listed in table 1 were found through continuation in Re_i, there is a small deviation in this parameter from that describing turbulent flow. This variation emulates the discrepancies one might see when comparing numerically computed solutions to turbulent flows in experiment.

5. Conclusions

We set out to determine whether ECSs of one type or another are present and being shadowed by turbulent flow in a geometry with continuous symmetries and boundary conditions exactly matching a realistic experimental set-up. Both questions were answered in the affirmative for a small-aspect-ratio TCF with counter-rotating cylinders. We found two dozen RPOs and TWs (not counting their symmetry-related copies) and determined that many of them are shadowed on accessible time scales, some rather frequently. The majority of ECSs we found are RPOs, so it is not surprising that it is this type of ECS that is shadowed the most frequently. What was unexpected is that the single most shadowed solution is a TW.

These results are quite significant, as they provide clear and unambiguous evidence supporting Hopf's picture of turbulence as a deterministic walk through neighbourhoods of various unstable solutions of the Navier–Stokes equation. The shadowing property implies that we can predict the evolution of turbulent flow over some interval of time, justifying the use of the ECS-based framework for a deterministic, dynamical description of turbulence. The length of this interval is not universal and is determined, as could be expected, by the degree of instability of the solution that is being shadowed.

Another key property of chaotic dynamics that has not been addressed fully is ergodicity. The number of ECSs we computed is insufficient for their neighbourhoods to cover any of the lobes of the chaotic set, so we cannot make any conclusive statements regarding this property, except for one. For ECSs embedded into both lobes 1 and 3, the number of unstable degrees is not constant. As shown by Kostelich *et al.* (1997), this implies that the dynamics are not uniformly hyperbolic in either lobe, so we should not expect the ergodic property to hold. This result is not exclusive to the flow we considered; the same observation applies to both pipe flow (Willis *et al.* 2013; Budanur *et al.* 2017), two-dimensional Kolmogorov flow (Chandler & Kerswell 2013; Lucas & Kerswell 2015) and its quasi-two-dimensional experimental realization Suri *et al.* (2018, 2020). The implications of this for a dynamical theory of turbulence remain unclear.

This study focused almost exclusively on the dynamical significance of various ECSs. In fact, an ECS-based framework can also be used to connect a deterministic, dynamical description of fluid turbulence with a more traditional, statistical description. In particular, partition of the chaotic set into neighbourhoods of various ECSs can be used to compute temporal means of any observable as a weighted sum over different ECSs. At present it remains unclear what types of ECSs should be included in the sum and how the weights should be computed. Initial studies (Kazantsev 1998; Chandler & Kerswell 2013; Lucas & Kerswell 2015) aiming to address such issues had various limitations and were

https://doi.org/10.1017/jfm.2021.522 Published online by Cambridge University Press

not conclusive, so further work in this area is needed. We will consider this issue in a subsequent publication.

Supplementary movies. Supplementary movies are available at https://doi.org/10.1017/jfm.2021.522.

Acknowledgements. The authors would like to thank M. Avila for sharing his TCF code.

Funding. The authors would like to gratefully acknowledge financial support by ARO under grant W911NF-15-1-0471 and by NSF under grant CMMI-1725587.

Declaration of interests. The authors report no conflict of interest.

Data availability statement. The data that support the findings of this study (relating to the exact coherent structures and their key properties) are openly available on GitHub at https://github.com/cdggt/tcf/tree/main/eta0.50.

Author ORCIDs.
Michael C. Krygier https://orcid.org/0000-0001-5729-8192;
Joshua L. Pughe-Sanford https://orcid.org/0000-0002-0208-2439;
Roman O. Grigoriev https://orcid.org/0000-0001-6220-4701.

References

Aitta, A., Ahlers, G. & Cannell, D.S. 1985 Tricritical phenomena in rotating Couette–Taylor flow. *Phys. Rev. Lett.* **54** (7), 673.

Allgower, E.L. & Georg, K. 2003 *Introduction to Numerical Continuation Methods*. SIAM.

Altmeyer, S., Do, Y., Marques, F. & Lopez, J.M. 2012 Symmetry-breaking Hopf bifurcations to 1-, 2-, and 3-tori in small-aspect-ratio counterrotating Taylor–Couette flow. *Phys. Rev.* E **86** (4), 046316.

Andereck, C.D., Liu, S.S. & Swinney, H.L. 1986 Flow regimes in a circular Couette system with independently rotating cylinders. *J. Fluid Mech.* **164**, 155–183.

Arnold, V.I. & Avez, A. 1968 *Ergodic Problems of Classical Mechanics*. W. A. Benjamin.

Auerbach, D., Cvitanović, P., Eckmann, J.-P., Gunaratne, G. & Procaccia, I. 1987 Exploring chaotic motion through periodic orbits. *Phys. Rev. Lett.* **58** (23), 2387.

Avila, M. 2012 Stability and angular-momentum transport of fluid flows between corotating cylinders. *Phys. Rev. Lett.* **108** (12), 124501.

Avila, M., Grimes, M., Lopez, J.M. & Marques, F. 2008 Global endwall effects on centrifugally stable flows. *Phys. Fluids* **20** (10), 104104.

Benjamin, T.B. & Mullin, T. 1981 Anomalous modes in the Taylor experiment. *Proc. R. Soc. Lond.* A **377** (1770), 221–249.

Budanur, N.B., Short, K.Y., Farazmand, M., Willis, A.P. & Cvitanović, P. 2017 Relative periodic orbits form the backbone of turbulent pipe flow. *J. Fluid Mech.* **833**, 274–301.

Buzug, T., Von Stamm, J. & Pfister, G. 1992 Fractal dimensions of strange attractors obtained from the Taylor–Couette experiment. *Physica* A **191** (1–4), 559–563.

Buzug, T., von Stamm, J. & Pfister, G. 1993 Characterization of period-doubling scenarios in Taylor–Couette flow. *Phys. Rev.* E **47** (2), 1054.

Chandler, G.J. & Kerswell, R.R. 2013 Invariant recurrent solutions embedded in a turbulent two-dimensional Kolmogorov flow. *J. Fluid Mech.* **722**, 554–595.

Chaté, H. & Manneville, P. 1987 Transition to turbulence via spatio-temporal intermittency. *Phys. Rev. Lett.* **58** (2), 112.

Cliffe, K.A. 1983 Numerical calculations of two-cell and single-cell Taylor flows. *J. Fluid Mech.* **135**, 219–233.

Coles, D. 1965 Transition in circular Couette flow. *J. Fluid Mech.* **21** (3), 385–425.

Cvitanović, P. 1988 Invariant measurement of strange sets in terms of cycles. *Phys. Rev. Lett.* **61** (24), 2729.

Cvitanović, P. 2013 Recurrent flows: the clockwork behind turbulence. *J. Fluid Mech.* **726**, 1–4.

Cvitanović, P. & Gibson, J.F. 2010 Geometry of the turbulence in wall-bounded shear flows: periodic orbits. *Phys. Scr.* **2010** (T142), 014007.

De Lozar, A., Mellibovsky, F., Avila, M. & Hof, B. 2012 Edge state in pipe flow experiments. *Phys. Rev. Lett.* **108** (21), 214502.

https://doi.org/10.1017/jfm.2021.522 Published online by Cambridge University Press

DEGUCHI, K. & ALTMEYER, S. 2013 Fully nonlinear mode competitions of nearly bicritical spiral or Taylor vortices in Taylor–Couette flow. *Phys. Rev.* E **87** (4), 043017.

DEGUCHI, K., MESEGUER, A. & MELLIBOVSKY, F. 2014 Subcritical equilibria in Taylor–Couette flow. *Phys. Rev. Lett.* **112** (18), 184502.

DENNIS, D.J.C. & SOGARO, F.M. 2014 Distinct organizational states of fully developed turbulent pipe flow. *Phys. Rev. Lett.* **113**, 234501.

ECKHARDT, B., FAISST, H., SCHMIEGEL, A. & SCHNEIDER, T.M. 2008 Dynamical systems and the transition to turbulence in linearly stable shear flows. *Phil. Trans. R. Soc.* A **366** (1868), 1297–1315.

ECKHARDT, B., SCHNEIDER, T.M., HOF, B. & WESTERWEEL, J. 2007 Turbulence transition in pipe flow. *Annu. Rev. Fluid Mech.* **39** (1), 447–468.

FIEDLER, B., SANDSTEDE, B., SCHEEL, A. & WULFF, C. 1996 Bifurcation from relative equilibria of noncompact group actions: skew products, meanders, and drifts. *Doc. Math.* **141**, 479–505.

FURUKAWA, H., WATANABE, T., TOYA, Y. & NAKAMURA, I. 2002 Flow pattern exchange in the Taylor–Couette system with a very small aspect ratio. *Phys. Rev.* E **65** (3), 036306.

GASPARD, P. 2005 *Chaos, Scattering and Statistical Mechanics*, vol. 9. Cambridge University Press.

HEISE, M., HOFFMANN, C., WILL, C., ALTMEYER, S., ABSHAGEN, J. & PFISTER, G. 2013 Co-rotating Taylor–Couette flow enclosed by stationary disks. *J. Fluid Mech.* **716**, R4.

HOCHSTRATE, K., ABSHAGEN, J., AVILA, M., WILL, C. & PFISTER, G. 2010 Decay of turbulent bursting in enclosed flows. In *7th IUTAM Symposium on Laminar-Turbulent Transition* (ed. P. Schlatter & D.S. Henningson), pp. 195–200. Springer.

HOF, B., VAN DOORNE, C.W.H., WESTERWEEL, J., NIEUWSTADT, F.T.M., FAISST, H., ECKHARDT, B., WEDIN, H., KERSWELL, R.R. & WALEFFE, F. 2004 Experimental observation of nonlinear traveling waves in turbulent pipe flow. *Science* **305** (5690), 1594–1598.

HOFFMANN, C., ALTMEYER, S., HEISE, M., ABSHAGEN, J. & PFISTER, G. 2013 Axisymmetric propagating vortices in centrifugally stable Taylor–Couette flow. *J. Fluid Mech.* **728**, 458–470.

HOPF, E. 1942 Abzweigung einer periodischen lösung von einer stationären lösung eines differentialsystems. *Ber. Math.-Phys. Kl Sächs. Akad. Wiss. Leipzig* **94**, 1–22.

HOPF, E. 1948 A mathematical example displaying features of turbulence. *Commun. Pure Appl. Maths* **1** (4), 303–322.

HUGUES, S. & RANDRIAMAMPIANINA, A. 1998 An improved projection scheme applied to pseudospectral methods for the incompressible Navier–Stokes equations. *Intl J. Numer. Meth. Fluids* **28** (3), 501–521.

HUSSAIN, A.K.M.F. 1983 Coherent structures–reality and myth. *Phys. Fluids* **26** (10), 2816–2850.

KAWAHARA, G. & KIDA, S. 2001 Periodic motion embedded in plane Couette turbulence: regeneration cycle and burst. *J. Fluid Mech.* **449**, 291–300.

KAWAHARA, G., UHLMANN, M. & VAN VEEN, L. 2012 The significance of simple invariant solutions in turbulent flows. *Annu. Rev. Fluid Mech.* **44**, 203–225.

KAZANTSEV, E. 1998 Unstable periodic orbits and attractor of the barotropic ocean model. *Nonlinear Process. Geophys.* **5**, 193–208.

KERSWELL, R.R. 2005 Recent progress in understanding the transition to turbulence in a pipe. *Nonlinearity* **18** (6), R17.

KERSWELL, R.R. & TUTTY, O.R. 2007 Recurrence of travelling waves in transitional pipe flow. *J. Fluid Mech.* **584**, 69–102.

KOLMOGOROV, A.N. 1941 The local structure of turbulence in incompressible viscous fluid for very large Reynolds numbers. *Dokl. Akad. Nauk SSSR* **30**, 301–305.

KOSTELICH, E.J., KAN, I., GREBOGI, C., OTT, E. & YORKE, J.A. 1997 Unstable dimension variability: a source of nonhyperbolicity in chaotic systems. *Physica* D **109** (1–2), 81–90.

KREILOS, T. & ECKHARDT, B. 2012 Periodic orbits near onset of chaos in plane Couette flow. *Chaos* **22** (4), 047505.

LAN, Y. 2010 Cycle expansions: from maps to turbulence. *Commun. Nonlinear Sci. Numer. Simul.* **15** (3), 502–526.

LORENZ, E.N. 1963 Deterministic non-periodic flow. *J. Atmos. Sci.* **20** (1), 30–41.

LORENZEN, A., PFISTER, G. & MULLIN, T. 1983 End effects on the transition to time-dependent motion in the Taylor experiment. *Phys. Fluids* **26** (1), 10–13.

LUCAS, D. & KERSWELL, R.R. 2015 Recurrent flow analysis in spatiotemporally chaotic 2-dimensional Kolmogorov flow. *Phys. Fluids* **27** (4), 045106.

MANDELBROT, B. 1967 How long is the coast of Britain? Statistical self-similarity and fractional dimension. *Science* **156** (3775), 636–638.

MARQUES, F. & LOPÉZ, J.M. 2006 Onset of three-dimensional unsteady states in small-aspect-ratio Taylor–Couette flow. *J. Fluid Mech.* **561**, 255–277.

https://doi.org/10.1017/jfm.2021.522 Published online by Cambridge University Press

MERCADER, I., BATISTE, O. & ALONSO, A. 2010 An efficient spectral code for incompressible flows in cylindrical geometries. *Comput. Fluids* **39** (2), 215–224.
MESEGUER, A., MELLIBOVSKY, F., AVILA, M. & MARQUES, F. 2009 Families of subcritical spirals in highly counter-rotating Taylor–Couette flow. *Phys. Rev.* E **79** (3), 036309.
MOODY, L.F. 1944 Friction factors for pipe flow. *Trans. ASME* **66**, 671–684.
MULLIN, T. 1982 Mutations of steady cellular flows in the Taylor experiment. *J. Fluid Mech.* **121**, 207–218.
MULLIN, T., TOYA, Y. & TAVENER, S.J. 2002 Symmetry breaking and multiplicity of states in small aspect ratio Taylor–Couette flow. *Phys. Fluids* **14** (8), 2778–2787.
NAGATA, M. 1990 Three-dimensional finite-amplitude solutions in plane Couette flow: bifurcation from infinity. *J. Fluid Mech.* **217**, 519–527.
NIKURADSE, J. 1932 Gesetzmassigkeiten der turbulenten stromung in glatten rohren. *Ver. Deutsch. Ing. Forsch.* **356**.
ORSZAG, S.A. & PATERA, A.T. 1983 Secondary instability of wall-bounded shear flows. *J. Fluid Mech.* **128**, 347–385.
PAGE, J. & KERSWELL, R.R. 2020 Searching turbulence for periodic orbits with dynamic mode decomposition. *J. Fluid Mech.* **886**, A28.
PARK, J.S. & GRAHAM, M.D. 2015 Exact coherent states and connections to turbulent dynamics in minimal channel flow. *J. Fluid Mech.* **782**, 430–454.
PFISTER, G., BUZUG, T. & ENGE, N. 1992 Characterization of experimental time series from Taylor–Couette flow. *Physica* D **58** (1–4), 441–454.
PFISTER, G., SCHMIDT, H., CLIFFE, K.A. & MULLIN, T. 1988 Bifurcation phenomena in Taylor–Couette flow in a very short annulus. *J. Fluid Mech.* **191**, 1–18.
PFISTER, G., SCHULZ, A. & LENSCH, B. 1991 Bifurcations and a route to chaos of an one-vortex-state in Taylor–Couette flow. *Eur. J. Mech. B/Fluids* **10** (2), 247–252.
SANDSTEDE, B., SCHEEL, A. & WULFF, C. 1999 Dynamical behavior of patterns with Euclidean symmetry. In *Pattern Formation in Continuous and Coupled Systems* (ed. M. Golubitsky, D. Luss & S.H. Strogatz), pp. 249–264. Springer.
SCHNEIDER, T.M., ECKHARDT, B. & VOLLMER, J. 2007 Statistical analysis of coherent structures in transitional pipe flow. *Phys. Rev.* E **75** (6), 066313.
SCHULZ, A., PFISTER, G. & TAVENER, S.J. 2003 The effect of outer cylinder rotation on Taylor–Couette flow at small aspect ratio. *Phys. Fluids* **15** (2), 417–425.
STREETT, C.L. & HUSSAINI, M.Y. 1991 A numerical simulation of the appearance of chaos in finite-length Taylor–Couette flow. *Appl. Numer. Maths* **7** (1), 41–71.
SURI, B., KAGEORGE, L., GRIGORIEV, R.O. & SCHATZ, M.F. 2020 Capturing turbulent dynamics and statistics in experiments with unstable periodic orbits. *Phys. Rev. Lett.* **125** (6), 064501.
SURI, B., TITHOF, J., GRIGORIEV, R.O. & SCHATZ, M.F. 2017 Forecasting fluid flows using the geometry of turbulence. *Phys. Rev. Lett.* **118** (11), 114501.
SURI, B., TITHOF, J., GRIGORIEV, R.O. & SCHATZ, M.F. 2018 Unstable equilibria and invariant manifolds in quasi-two-dimensional Kolmogorov-like flow. *Phys. Rev.* E **98** (2), 023105.
TSAMERET, A. & STEINBERG, V. 1994 Competing states in a Couette–Taylor system with an axial flow. *Phys. Rev.* E **49** (5), 4077.
VAN VEEN, L., KIDA, S. & KAWAHARA, G. 2006 Periodic motion representing isotropic turbulence. *Fluid Dyn. Res.* **38** (1), 19–46.
VISWANATH, D. 2007 Recurrent motions within plane Couette turbulence. *J. Fluid Mech.* **580**, 339–358.
VISWANATH, D. 2009 The critical layer in pipe flow at high Reynolds number. *Phil. Trans. R. Soc. Lond.* A **367**, 561–576.
VON KÁRMÁN, T. 1930 Mechanische ahnlichkeit und turbulenz. *Math. Phys. Klasse*. 58–76.
WALEFFE, F. & WANG, J. 2005 Transition threshold and the self-sustaining process. In *IUTAM Symposium on Laminar-Turbulent Transition and Finite Amplitude Solutions* (ed. T. Mullin & R. Kerswell), pp. 85–106. Springer.
WILLIS, A.P., CVITANOVIĆ, P. & AVILA, M. 2013 Revealing the state space of turbulent pipe flow by symmetry reduction. *J. Fluid Mech.* **721**, 514–540.
YALNIZ, G., HOF, B. & BUDANUR, N.B. 2020 Coarse graining the state space of a turbulent flow using periodic orbits. *Phys. Rev. Lett.* **126**, 244502.

https://doi.org/10.1017/jfm.2021.522 Published online by Cambridge University Press